Information Fusion 129 (2026) 103970

Contents lists available at ScienceDirect

Information Fusion

journal homepage: www.elsevier.com/locate/inffus

Enhancing structural condition assessment in steel pipelines via a WGAN-AAE data fusion methodology

Sahar Hassani [a,*], Samir Mustapha [b], Mohsen Mousavi [a], Jianchun Li [c], Chongmin Song [a], Ulrike Dackermann [a,*]

[a] Centre for Infrastructure Engineering and Safety, School of Civil and Environmental Engineering, University of New South Wales, Sydney, NSW, Australia
[b] Department of Mechanical Engineering, Laboratory of Smart Structures and Structural Integrity (SSSI), American University of Beirut, Beirut, Lebanon
[c] School of Civil and Environmental Engineering, University of Technology Sydney, 2007, Ultimo, NSW, Australia

ARTICLE INFO

Keywords:
Pipe condition monitoring
Wasserstein generative adversarial network
Adversarial autoencoder
Data fusion
Deep learning

ABSTRACT

Pipelines for water and oil transport are vulnerable to ageing, operational loads, and harsh environments, necessitating reliable condition monitoring. This study presents a hybrid sensing and data-driven framework for accurate leak detection and localisation in steel pipelines instrumented with Fibre Bragg Grating (FBG) sensors. For the research, a 6 m steel pipe was instrumented with FBG sensors placed longitudinally and circumferentially to quantify strain responses under various leakage and operating conditions. The study evaluates the sensitivities of the FBG strain recordings to variations in leak size, leak location, pressure and flow. A hybrid WGAN-AAE data fusion methodology is proposed to analyse limited and noisy strain data for accurate classification of leakages, flow rate and pressure. The framework integrates a Wasserstein GAN (WGAN) that generates synthetic FBG signals tuned to the operating envelope; an adversarial autoencoder (AAE), which provides domain-aware latent regularisation and learned feature-level fusion of real and synthetic data; and a 2D-Convolutional Neural Network classifier that operates on the fused representations. Models are trained on 70 % real data augmented with WGAN samples and evaluated on the remaining 30 % real data. The study addresses both single-label (pressure, flow, leak size, leak location) and multi-label classification based on a Binary Relevance approach. The classifiers achieved a 94.89 % ± 1.13 % accuracy for multi-label classification on the test set based on real data. Additionally, single classification tasks show high accuracy rates, with 91.04 % ± 0.90 % for flow rate classification, over 98.69 % ± 0.93 % for pressure classification, 100 % ± 0.00 % for leakage size classification, and 91.22 % ± 0.98 % for leakage localization. A comparative analysis of leakage-location classification across the ten best sensor layouts shows that WGAN + AAE outperforms GAN + AAE and WGAN-concatenation baselines, supporting the benefits of Wasserstein synthesis, latent regularisation, and learned fusion. These results demonstrate that the proposed hybrid sensing and data-fusion approach enables accurate and robust leak detection and localisation in pipeline systems, even with limited datasets and under noisy, variable operating conditions.

1. Introduction

The use of pipelines to transport hazardous materials, such as crude oil and refined petroleum products, is widespread owing to their functionality, efficiency, and cost-effectiveness [1]. Compared with alternative transport modes [2], pipelines offer practical and economical solutions for both short-distance transfers within refineries and neighbouring facilities and long-distance transmission. They also convey oil and gas from numerous wells, including those in remote or challenging terrain [3]. The vast reach of pipeline infrastructure exposes it to diverse failure modes. Such incidents can lead to loss of transported materials and pose serious health and environmental risks [4]. The consequences depend on factors such as the pipeline's location and the substance being transported, with potential disruption to economic activity, ecological damage, and public-health impacts. A notable case is the Keystone spill in North Dakota, where approximately 1.4 million litres of a bitumen-diluent mixture were released [5]. The diluent vapourised into the atmosphere, dispersing harmful compounds, while the residual bitumen contaminated the soil and produced a strong odour. Similar events in 2019, including spills of about 120,000 litres in Garfield County

* Corresponding authors.
E-mail address: sahar.hassani@unsw.edu.au (S. Hassani).

https://doi.org/10.1016/j.inffus.2025.103970
Received 23 July 2025; Received in revised form 29 October 2025; Accepted 17 November 2025
Available online 22 November 2025

(Oklahoma), 300,000 litres in Miller Grove (Texas), and 40,000 litres in Alberta (Canada), underscore the widespread and damaging nature of such failures [6].

Common leak-detection techniques rely on external sensors, including negative pressure waves (NPW), ultrasonic testing, eddy-current analysis, and electromagnetic flux-leakage methods [7]. These approaches can be deployed without interrupting operations and yield quantifiable results. For example, Jin et al. [8] used acoustic and pressure sensors mounted on the pipe surface to identify leaks along a 170-kilometre gas pipeline, achieving a localisation error of about 720 metres. Beyond sensor-based methods, model-driven techniques [9] simulate pipeline behaviour under conditions such as valve operations or flow changes and compare measured flows with model predictions. Despite their effectiveness, these methods require precise input data and substantial computational resources to deliver timely, reliable results.

Spirin et al. [10] developed a polymer-based casing that detects petroleum hydrocarbons (e.g., petrol/gasoline) via reversible swelling upon contact. The resulting expansion alters the strain on an attached Fibre Bragg Grating (FBG) sensor, enabling leak detection. A key limitation-particularly for large-scale pipeline systems-is that the leaking fluid must be in close proximity to the sensor for the polymer coating to respond. To mitigate this constraint, Lee and Tsuda [11] proposed a hybrid system combining piezoelectric (PZT) wafers with FBG sensors along a fibre-optic cable. In this design, an acoustical wave is launched and propagates along the fibre; the segment between the transmitter and the FBG serves as the sensing region. A drop in amplitude indicates that leaked liquid is interfering with wave propagation, signalling a leak. While this hybrid approach improves detection capability, it partly offsets the usual advantages of fibre-optic systems because it requires electrical connections along the pipeline to power the PZT elements.

Artificial intelligence (AI) has demonstrated strong utility across different areas like engineering, medicine, finance, and cybersecurity by improving detection accuracy, robustness, and scalability [12–21]. Techniques such as data augmentation, feature-level fusion of heterogeneous sensor networks, transfer learning from related domains, and multi-label learning to capture interdependent attributes have repeatedly boosted performance in real-world settings [13]. Complementary practices, uncertainty calibration, active learning for targeted labelling, and domain-aware regularisation further reduce false alarms and improve generalisation under shifting operating conditions [14]. Leveraging these AI advances within our framework enhances accuracy and reliability for pipeline anomaly detection while maintaining practical efficiency [12]. Machine Learning (ML) models have become a vital tool for monitoring pipeline systems, improving efficiency and consistency [22,23]. Automated detection typically begins by extracting signal features indicative of faults or leaks. One major class of models targets structural defects-whether or not they cause immediate leakage-thereby covering a broader range of faults. For example, Khodayari-Rostamabad et al. [24] developed a classifier using magnetic flux-leakage data that detected cracks and material loss with 97.7 % accuracy and a separate model to quantify damage extent with 98.3 % accuracy. Beyond pipelines, ML has been applied to crack identification in self-healing concrete [25] and to modelling complex material behaviours, such as using deep neural networks to capture the flexoelectric response of compressed pyramid-shaped nanostructures [26].

With their strong capabilities in processing spatial data and recognizing complex patterns, Convolutional Neural Networks (CNNs) have become increasingly popular in leak detection across different industries [13,27]. These deep learning models are particularly effective at identifying anomalies in pipeline systems by analyzing variations in signals such as pressure, temperature, and acoustics. For example, Zhang et al. [28] applied a CNN model with transfer learning using the VGGish architecture to classify acoustic recordings from a Smart Water Network (SWN) in Adelaide. In order to distinguish routine events from irregular events, the system detected anomalies, which were then used to activate a Siamese CNN. This approach achieved a validation accuracy of 92.44 %, demonstrating its potential for early detection of leaks and structural cracks in water pipelines.

By combining information from multiple sources, data fusion enhances the accuracy and robustness of pipeline leak-detection systems [29]. A variety of fusion strategies integrate data gathered from different sensor types. Sensor-level fusion merges outputs from devices such as FOS and pressure transducers to provide a more complete picture of the pipeline's condition. Modal (modality-level) fusion blends data from different measurement modalities to strengthen fault assessment. Machine-learning techniques, such as adversarial autoencoders (AAEs), integrate multiple sources of leakage information into a unified representation, enabling deeper insight into leakage characteristics. Conti et al. [30] synthesised acoustic and pressure signals using a dual-Pearson threshold-ensemble empirical mode decomposition (DP-EEMD) algorithm for noise reduction, achieving 98.3 % classification accuracy and surpassing single-sensor strategies. In leakage monitoring, three prominent fusion levels are commonly adopted: sensor-level fusion [31], which combines raw sensor inputs; decision-level fusion [32], which integrates outputs from multiple classifiers or models; and feature-level fusion [33], which merges key features to form more informative inputs for downstream analysis. Combining these approaches enables more precise and resilient leakage detection under varying operational conditions.

A well-balanced dataset is essential for successful machine-learning-based leakage detection, as class balance underpins effective classification. However, collecting sufficient abnormal data–particularly from real-world structures–can be challenging. To address this, techniques for generating synthetic fault data [26] are valuable for augmenting datasets and improving model accuracy. Wasserstein Generative Adversarial Networks (WGANs) [34] are especially useful in this context, producing realistic synthetic samples that closely mirror true leakage scenarios. By learning the distribution of healthy operational data, WGANs can create a wide range of artificial anomalies that enhance model generalisation. Compared with traditional GANs, WGANs alleviate mode collapse and stabilise training, yielding more diverse and reliable data. They also improve representation of the feature space, facilitating more accurate separation between normal and faulty conditions.

This current study employs a distributed FBG sensing system to monitor the structural and operational state of steel pipelines. This research aims to: (i) design and implement advanced data analysis algorithms including a 2D-CNN and a novel WGAN-AAE fusion framework-applied to FBG data; (ii) assess the performance of FBG-based strain sensing for evaluating structural integrity and operating conditions under limited and noisy data; (iii) investigate how sensor quantity and orientation affect classification accuracy; (iv) analyse the influence of varying flow and leakage scenarios on measured surface strain; and (v) develop an automated condition-monitoring framework that first fuses generated and real data, then extracts informative features from the fused representation, and finally performs the classification task.

This paper introduces the following three key innovations:

- We present a novel two-stage generative-representation learning framework tailored to small, noisy FBG datasets and varying operating conditions. In the first stage, a WGAN synthesises FBG signals that are explicitly tuned to the observed operating envelope; the Wasserstein objective with Lipschitz controls provides smooth gradients and mitigates mode collapse, helping the generator cover rare regimes that are critical for leakage analysis. In the second stage, an AAE performs domain-aware latent regularisation and learned feature-level fusion of real and synthetic signals. Rather than naively concatenating raw data, the AAE shapes a latent space aligned with an explicit prior and emphasises discriminative structures linked to pressure, flow, leak size, and leak location. This staged fusion maximises information extraction when real anomalies are scarce and sensor noise is non-trivial.

- We deploy FBG sensors longitudinally and circumferentially to capture directional strain responses induced by hydraulic and structural changes. Controlled experiments on a 6 m steel pipeline testbed quantify how operating parameters imprint on the strain field: a 0.2 bar pressure increase produces an ≈20 % larger strain-drop amplitude; a +5 GPM flow increment reduces the drop by ≈5–6 %; and larger leaks (2–5 cm^2) yield ≈55 % greater drops than small leaks. The resulting dataset spans flow, pressure, leak size, and location regimes, enabling rigorous validation and ablation of sensor layouts, including the ten best-performing configurations used in our comparative analysis.
- We employ a 2D–CNN operating on fused WGAN–AAE representations to solve both single-label tasks (pressure, flow, leak size, leak location) and a realistic multi-label setting in which all attributes are predicted jointly. The training protocol uses 70 % of the real data (with WGAN augmentation applied only to the training split), consistent preprocessing, and Binary Relevance for multi-label inference; cross-validation confirms robustness and high accuracy across different splits. The remaining 30 % of the data, not used for training the WGAN, is held out for testing.

2. Proposed methodology

The following sections detail the study methodology. We introduce a WGAN-AAE fusion approach that integrates WGAN and AAE, describe the FBG-instrumented testbed, and outline investigated the leakage scenarios. We also present the development of classifiers for both multi-label and single-label tasks.

2.1. FBG-based sensing

In this work, strain was measured using FBG sensors. FBG sensing was selected due to its immunity to EMI (Electromagnetic Interference), passive operation at the sensing point, and scalability via wavelength-multiplexing, which together enabled kilometre-scale, real-time monitoring of industrial pipelines [12,29]. Compared with conventional electrical gauges/IEPE (Integrated Electronics Piezo-Electric) sensors, FBGs reduce cabling and powered field hardware, tolerate harsh environments when properly protected, and provide kHz-rate interrogation with microstrain-level resolution. In this experimental setup, longitudinal and circumferential gratings were bonded using weldable/adhesive carriers and protected by armoured jackets, allowing robust operation under temperature, humidity, and chemical exposure conditions typical of pipeline facilities [29,35].

An FBG consists of periodic gratings inscribed in an optical fiber [12,36,37]. When illuminated with broadband light, the grating reflects a narrow band at the Bragg wavelength, while the remaining spectrum propagates along the fibre to downstream sensors [36]. Mechanical strain and temperature shifts change the Bragg wavelength, which is given by:

$$\lambda_b = 2 \cdot n_{\text{eff}} \cdot \tau \tag{1}$$

where λ_b denotes the Bragg wavelength, n_{eff} is the effective refractive index of the fiber core, and τ is the periodic spacing of the grating structure.

Variations in grating spacing, caused by mechanical strain or temperature fluctuations, produce a detectable shift in the reflected wavelength measured by the interrogation unit. The sensor's response to an applied strain (ε) can be expressed as the relative change in the Bragg wavelength, $\left(\frac{d\lambda_b}{\lambda_b}\right)$, governed by changes in both the effective refractive index (dn_{eff}) and the grating period ($d\tau$), as follows:

$$\frac{d\lambda_b}{\lambda_b} = \frac{dn_{\text{eff}}}{n_{\text{eff}}} + \frac{d\tau}{\tau} \tag{2}$$

In Eq. (2), the term $\frac{dn_{\text{eff}}}{n_{\text{eff}}}$ can be written as

$$\frac{n_{\text{eff}}^2}{2}\left[p_{12} - \nu\,(p_{11} + p_{12})\right]\varepsilon,$$

where ν is the Poisson's ratio of the material and p_{11}, p_{12} are the strain-optic coefficients from the photoelastic (Pockels) tensor. Moreover, the relative change in grating period $\frac{d\tau}{\tau}$ can be replaced by the axial strain ε. Combining these expressions and collecting constants yields the following relationship between the Bragg-wavelength shift and the applied strain:

$$\frac{d\lambda_b}{\lambda_b} = K_\epsilon \epsilon \tag{3}$$

Here, $K_\epsilon = 1 + \frac{n_{\text{eff}}^2}{2}\left[p_{12} - \nu(p_{11} + p_{12})\right]$ represents the strain sensitivity coefficient of the FBG sensor. It is the only constant in the equation and encapsulates how the Bragg wavelength responds to applied strain.

For temperature sensing (T), analogous derivations can be carried out by accounting for the thermal-optical tensor ζ and the fibre's thermal expansion coefficient α.

$$d\lambda_b = 2\left(\tau\frac{dn_{\text{eff}}}{dT} + n_{\text{eff}}\frac{d\tau}{dT}\right)dT \tag{4}$$

$$\frac{d\lambda_b}{\lambda_b} = \left(\underbrace{\frac{1}{n_{\text{eff}}}\frac{dn_{\text{eff}}}{dT}}_{\zeta} + \underbrace{\frac{1}{\tau}\frac{d\tau}{dT}}_{\alpha}\right)dT \tag{5}$$

$$\frac{d\lambda_b}{\lambda_b} = (\zeta + \alpha)\,dT \tag{6}$$

The term in the bracket of (6) represents the temperature sensitivity of the FBG. Therefore, one can obtain a correlation between the FBG temperature and the associated wavelength shift as follows:

$$\frac{d\lambda_b}{\lambda_b} = K_T\,dT \tag{7}$$

where K_T serves as the sole constant in the equation characterizing the temperature sensitivity of the fibre.

In this study, strain variations were measured directly using FBG sensors mounted on the pipe surface. The array included standard FBG strain sensors and temperature, compensated variants to minimise thermal effects. In the compensated sensors, two FBGs are integrated: one is bonded to the structure to record mechanical strain, and the other is isolated on a separate metal substrate to record temperature. The interrogation system computes temperature-compensated strain from the reflected wavelengths of both FBGs, together with known material properties, following the theoretical relationships introduced earlier. We conducted a series of experiments to collect FBG strain data under varied conditions-pressure, flow rate, leakage location, and hole size, with the goal of simulating realistic pipeline leakage scenarios. To study the effect of sensor placement on measurement and analysis, FBG sensors were installed both longitudinally and circumferentially at different positions and orientations. During each test, all sensors recorded simultaneously, ensuring consistency and avoiding parameter drift. Fibres were bonded directly to the pipe surface so that measured strain reflected internal flow conditions, and the full dataset was acquired via FBG interrogation systems. By systematically varying flow and leakage parameters across trials, we quantified their effects on the measured signals.

2.2. Proposed fusion framework

This paper introduces a novel fusion of WGAN and AAE, forming a WGAN-AAE framework for generating highly informative fused data for leakage detection. In the following sub-sections, we provide a detailed introduction to AAE and WGAN individually, highlighting their complementary capabilities. The sub-section outline that, in the proposed

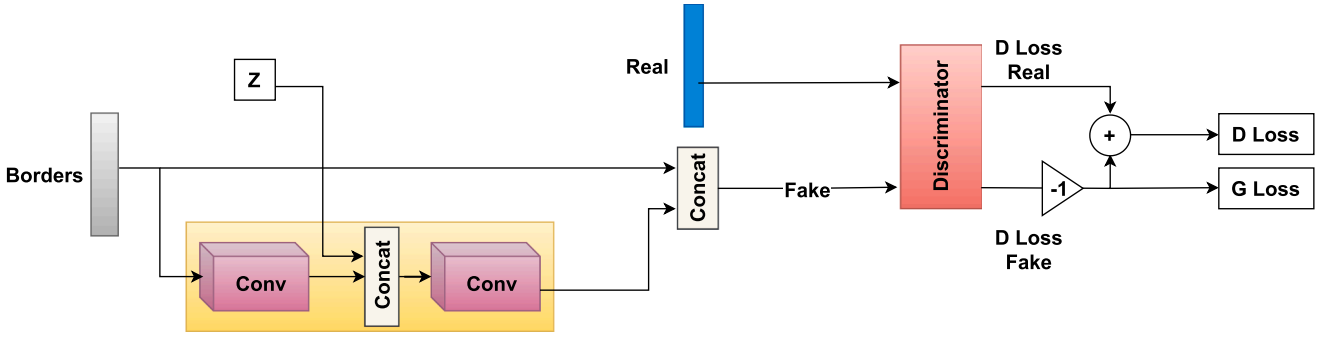

Fig. 1. WGAN architecture.

Table 1
WGAN hyperparameters.

Hyperparameter	Value	Description
Latent dimension (`latent_dim`)	100	Size of the random noise vector.
Feature dimension (`feature_dim`)	varies	Size of the feature vector in the input data.
Generator activation	`relu`	Activation function for the generator's hidden layers.
Critic activation	`relu`	Activation function for the critic's hidden layers.
Generator output activation	`linear`	Activation function for the generator's output layer.
Learning rate (Adam)	0.001	Learning rate for the Adam optimiser.
Batch size	50	Number of samples per mini-batch.
Epochs	1000	Total number of training epochs.
Weight clipping	0.01	Clip value applied to critic weights (WGAN Lipschitz constraint).

framework, the data is first concatenated, then augmented with WGAN-generated samples, and finally fused via an AAE to extract informative features and integrate real and synthetic data. This end-to-end procedure constitutes the fusion stage of our anomaly-detection framework.

2.2.1. WGAN architecture

WGAN [34] represent an advanced subset of the broader class of Generative Adversarial Networks (GANs) [14,38,38–40]. GANs operate through a competitive framework involving two neural networks: a generator, which produces synthetic data intended to mimic the real data distribution, and a discriminator, which evaluates whether given samples are real or generated. As a result of the introduction of WGANs, several challenges associated with traditional GANs have been addressed, such as unstable training behavior and mode collapse. A WGAN uses Wasserstein distance as a loss function to provide a smoother and more informative gradient, resulting in improved training stability and sample diversity.

WGANs are designed to minimize the Wasserstein distance between the distribution of real data and the distribution generated by the model. This is accomplished through an adversarial training process, where the generator (G) is tasked with producing realistic samples, and the critic (D)-which replaces the traditional discriminator-evaluates the Wasserstein distance rather than performing binary classification. The learning process is formulated as a minimax optimization problem [34]:

$$\min_{G} \max_{D \in D} \mathbb{E}_{x \sim P_r}[D(x)] - \mathbb{E}_{\tilde{x} \sim P_g}[D(\tilde{x})] \tag{8}$$

where D denotes the set of 1-Lipschitz functions, and P_g represents the model (generated) distribution, implicitly defined by $\tilde{x} = G(z)$ with $z \sim p(z)$. In this framework, assuming an optimal critic (used instead of a discriminator, as it is not performing binary classification), minimizing the loss with respect to the generator's parameters effectively reduces the Wasserstein distance $W(P_r, P_g)$ between the real and generated distributions. The generator aims to minimize discrepancies between generated and real samples, while the critic aims to maximize them, acting as an estimator for the Wasserstein distance. In this paper, we apply Lipschitz constraints via weight clipping (clip = 0.01) to stabilize critic training.

The training process updates the generator and critic parameters according to the WGAN objective. The generator produces samples that resemble real data, while the critic provides a meaningful estimate of the Wasserstein distance. Both networks are trained iteratively, refining the generator's ability to create realistic samples and the critic's ability to estimate distance. In this work, a WGAN was used to generate synthetic data that reflected the underlying distribution of the real dataset. An overview of the architecture and training is as follows:

- We used a custom Wasserstein loss to train the critic, guiding the generator toward samples that closely match the real distribution.
- For each training iteration, 70 % of the real dataset was loaded; these samples were processed and standardised using StandardScaler from the scikit-learn library.
- The generator takes random noise and real features as input and outputs generated features (see Fig. 1); the critic is tasked with distinguishing real from generated samples.
- The generator, critic, and the combined WGAN model were built and compiled with the Wasserstein loss and the Adam optimiser.
- Training proceeded by alternating critic and generator updates; the generator aimed to produce synthetic samples that the critic could not easily distinguish from real samples.
- After each iteration, weight clipping was applied to the critic to enforce the 1-Lipschitz constraint and stabilise training.
- During training, we monitored the Wasserstein losses for real and generated samples as well as the generator loss; optionally, synthetic samples and model checkpoints were saved for analysis.

Table 1 lists the hyperparameters used for the WGAN architecture.

2.2.2. AAE architecture

The AAE [41] is an extension of the conventional autoencoder architecture, incorporating elements of adversarial training to improve the learning of a meaningful and structured representation of latent code. To increase the ability to learn and generalize, an ensemble of autoencoders is used. An ensemble of autoencoders can capture different aspects of the input data, contributing to a more robust representation. Multi-autoencoder ensembles are created by training them independently and then aggregating their outputs during inference.

Table 2
Architecture and hyperparameters of the AAE approach.

Component	Hyperparameters
Data Scaling	Min-Max Scaler
Train-Test Split	Test size: 0.30, Random state: 10
Encoder	Dense layers: 128, 64 Activation function: ReLU Batch Normalization
Bottleneck	Dense layer: 300
Decoder	Dense layers: 64, 128 Activation function: ReLU Batch Normalization
Output Layer	Activation function: Linear
Autoencoder Model	Adam optimizer, Loss: Mean Squared Error (MSE), Metrics: Accuracy
Discriminator Model	Adam optimizer, Learning rate: 0.0002 Beta 1: 0.5 Loss: Binary Crossentropy, Metrics: Accuracy
Adversarial Model	Adam optimizer Loss weights: [0.9, 0.1] Loss: [MSE, Binary Crossentropy]
Training	Epochs: 800-1000, Batch size: 32

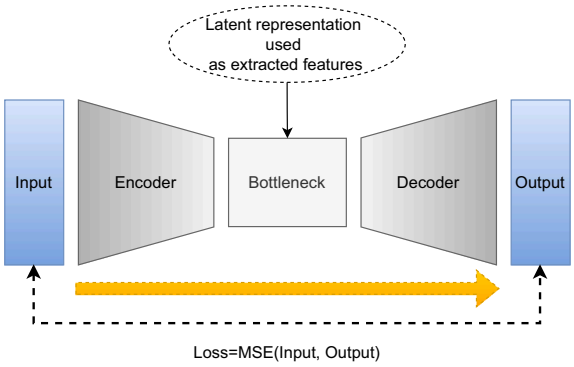

Fig. 2. Flowchart of the feature extraction process from an AAE model.

Let x denote the input data and z represent the latent code (hidden representation) produced by an autoencoder comprising a deep encoder and decoder network. The prior distribution of the target over the latent space is denoted by $p(z)$, while the encoder defines the conditional distribution $q(z|x)$, and the decoder models $p(x|z)$, the likelihood of reconstructing the input. Furthermore, $p_d(x)$ refers to the true data distribution and $p(x)$ represents the learned distribution of the model over the input space. The encoding function $q(z|x)$ induces an aggregated posterior over the latent space, defined as [41]:

$$q(z) = \int q(z|x) \cdot p_d(x)\, dx \tag{9}$$

The AAE is an enhanced version of a conventional autoencoder, incorporating a regularisation mechanism that aligns the aggregated posterior $q(z)$ with a specified prior distribution $p(z)$. This alignment is achieved by integrating an adversarial network into the latent space of the autoencoder. While the autoencoder focuses on minimising reconstruction loss, the adversarial network encourages the latent distribution $q(z)$ to resemble the desired prior $p(z)$. In this setup, the encoder $q(z|x)$ simultaneously functions as the generator in the adversarial framework, attempting to produce latent codes that the discriminator cannot distinguish from samples drawn from $p(z)$.

Stochastic gradient descent (SGD) trains both the autoencoder and the adversarial components in two alternating stages per mini-batch: reconstruction and regularisation. In the reconstruction stage, the autoencoder updates the encoder and decoder to minimise the difference between the input and its reconstruction. In the regularization phase, the discriminator of the adversarial network is first trained to differentiate between true prior samples and latent codes generated by the encoder. Then, the encoder is updated to generate latent representations that mislead the discriminator, effectively pushing $q(z)$ closer to $p(z)$. After training, the decoder learns a generative mapping from the prior distribution $p(z)$ to the data space, enabling it to generate realistic samples consistent with the original data distribution. Fig. 2 presents an overview of the typical architecture used in an AAE model.

The AAE used in this study comprises three components: an encoder, a decoder, and a discriminator. It enables unsupervised learning by coupling autoencoder reconstruction with adversarial regularisation for latent-space shaping. Activation functions are chosen to support stable training and expressive representations. The encoder and decoder hidden layers use ReLU activations to introduce nonlinearity and capture complex patterns; the decoder output uses a linear activation to predict continuous values. In the discriminator, ReLU is applied to hidden layers to model structure in the bottleneck representation, and a sigmoid activation is used at the output to yield probabilities for binary discrimination. Together, these choices enhance the model's representational power and training behaviour. Using an AAE enables several key objectives: (1) dimensionality reduction, (2) denoising, (3) feature extraction, and (4) input fusion [14,42]. The AAE facilitates effective fusion by integrating heterogeneous raw inputs into a shared latent representation, producing an integrated dataset. This, in turn, supports more comprehensive analysis and a holistic understanding of information drawn from diverse data sources. Table 2 summarises the architecture and hyperparameters, including preprocessing, model components, and training configurations.

2.3. Two-dimensional convolutional neural networks (2D-CNNs)

CNNs are specialized feed-forward neural networks that automatically learn features by adjusting filters, addressing issues such as vanishing and exploding gradients [13,43,44]. There are three layers in this CNN architecture: convolutional, pooling, and fully connected. To produce feature maps, input data is transformed into tensors and processed through convolutional layers. As a result, these layers enhance the recognition of objects and digits without the need for manual selection. In order to achieve shift invariance and efficiency, convolution layers are followed by pooling layers, which reduce feature map resolution, and finally by fully connected layers. An output layer for classification typically uses a softmax function, while an output layer for regression uses a regression function. In addition to image recognition, CNNs can also be applied to one-dimensional signals using a 1D-CNN. Due to their ability to capture spatial hierarchies, 2D-CNNs are particularly useful for computer vision tasks. For non-linearity, they employ activation functions like ReLU and filters to detect local features in 2D data. With pooling layers, computational complexity is reduced while important features are retained, and overfitting is prevented with techniques like dropout.

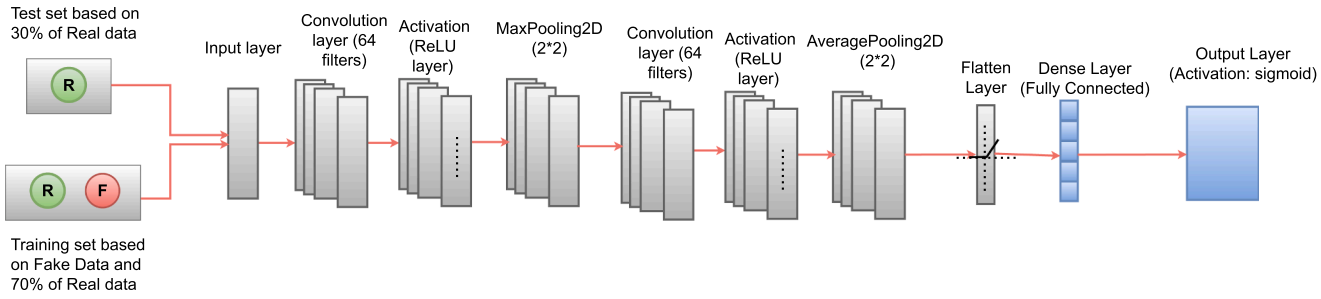

Fig. 3. Proposed 2D-CNN architecture for classification tasks.

The ability to capture intricate spatial patterns makes 2D-CNNs essential for tasks such as image classification and object detection [44,45]. This paper uses a 2D-CNN framework to classify pipe conditions. The model architecture is depicted in Fig. 3. Inputs of the 2D-CNN model are fusions of denoised real and synthetic strains for training and denoised and merged real strains for testing.

In this work, we use a 2D-CNN algorithm to classify pressure, flow rate, leak location, and leak size. As a result, the problem of this paper is a multi-label classification problem. Among classification tasks, a fundamental distinction exists between simple (single-label) classification and multi-label classification. In traditional single-label classification, each instance in the dataset is associated with a unique class, and the primary objective is to assign that instance to the most appropriate category. This binary or categorical assignment is straightforward, as each instance is considered to belong to a single and mutually exclusive class. Conversely, multi-label classification [46] extends this paradigm to scenarios where instances may exhibit multiple characteristics simultaneously. In multi-label classification, an instance can be associated with more than one class, allowing for a nuanced representation of complex relationships within the data. This paradigm shift introduces a richer and more flexible framework, enabling the modelling of intricate scenarios where instances possess diverse attributes or attributes that overlap across multiple categories. The adaptation from a singular, exclusive assignment to a more inclusive and layered classification approach in multi-label tasks acknowledges and accommodates the multifaceted nature of real-world datasets, where instances often embody multiple characteristics concurrently. Fig. 4 illustrates three distinct classification scenarios: binary, multiclass, and multi-label. In the binary classification subplot, two classes are differentiated by color, demonstrating a clear decision boundary. The multiclass subplot extends the complexity with three classes and a more intricate decision boundary. The multi-label subplot highlights instances belonging to multiple classes, emphasizing the versatility of ML in handling diverse classification tasks.

2.3.1. Binary relevance (BR) method

In this paper, we employ the Binary Relevance (BR) method for multi-label classification [47–52]. The BR strategy reduces a multi-label problem with m labels to m independent binary classification problems. More precisely, it induces m hypotheses $h_1, h_2, \ldots, h_m$, each responsible for predicting the relevance of a single label, using the same input space $\mathcal{X}$ [52]:

$$h_j : \mathcal{X} \to \{0,1\}, \quad j = 1, \ldots, m.$$

Labels are thus predicted independently, and potential dependencies among labels are not explicitly modelled. Despite this limitation, BR offers several advantages: (i) any binary learning method can serve as the base learner, (ii) the computational complexity scales linearly with the number of labels, and (iii) training can be parallelised easily. In practice, BR attains competitive results on benchmark datasets when paired with state-of-the-art base learners and appropriate hyperparameter tuning, and it has been shown theoretically and empirically to perform strongly for decomposable loss functions [51,52].

From a probabilistic perspective, if each binary model h_j provides calibrated estimates of the marginal probability $P(y_j = 1 \mid \mathbf{x})$, then BR is well suited to losses whose risk minimiser depends only on label-wise marginals. Since each binary learner typically optimises per-label accuracy, the aggregate BR model naturally minimises the Hamming loss:

$$\text{HammingLoss}(\mathbf{y}, h(\mathbf{x})) = \frac{1}{m}\sum_{j=1}^{m} \mathbf{1}\big[y_j \neq h_j(\mathbf{x})\big],$$

which averages the $0/1$ error across the m labels and equals the proportion of labels predicted incorrectly. With appropriate base learners, BR can also perform well on other macro-averaged label-based metrics, such as macro-F1 [49].

On the other hand, BR's decomposition is suboptimal for metrics whose risk minimisation requires modelling the joint label distribution:

$$\text{Subset}_{0/1}(\mathbf{y}, h(\mathbf{x})) = \mathbf{1}\big[\mathbf{y} \neq h(\mathbf{x})\big].$$

In these cases, algorithms that estimate (or approximate) joint label probabilities are preferable to achieve optimal performance. Each classifier produces a probability via a sigmoid output and is trained with binary cross-entropy; the overall objective is the sum of per-label losses, optimised with stochastic gradient descent. At inference, we threshold the predicted probabilities to obtain binary decisions. This setup is simple and scalable, provides label-specific decision boundaries, and is well suited to our dataset's heterogeneity, while acknowledging that it does not explicitly model label dependencies.

The data classification process in our study involves a dual approach. Firstly, individual classifiers are established and evaluated for each parameter, namely pressure, flow rate, leakage size, and location. This allows for a detailed assessment of each parameter's impact on classification accuracy. Secondly, a more comprehensive approach is undertaken by combining the classifiers established for each parameter. This holistic approach referred to as multi-label class classifications, involves the classification of testing data by utilizing a combination of classifiers from the individual parameters. To facilitate the classification process, sensor data from each experiment is organized into a 1*120,000 array. These arrays, corresponding to each experiment, are then concatenated to create a final 720*120,000 array. The fusion of real and synthetic data is achieved through the proposed WGAN-AAE approach, resulting in 300 reduced and fused features from each sensor combination. The aim is to identify the most effective combination of sensors for accurate classification, specifically targeting leakage detection. In order to enhance the model's robustness, we introduce synthetic data generated using a WGAN on 70 % of the training data. This synthetic data, combined with the actual 70 % of real data, formed the training dataset. Subsequently, the model was tested on the remaining 30 % of real data that had been initially set aside. Cross-validation is performed to ensure that the proposed approach is capable of training on various data splits, promoting fairness and reliability in the evaluation process. This comprehensive

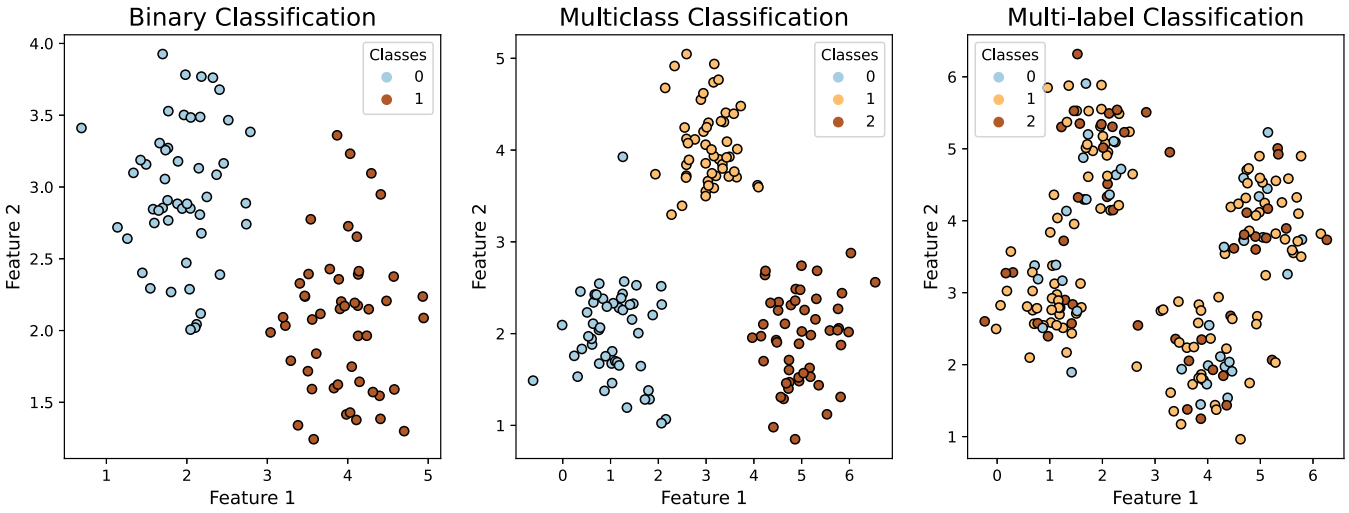

Fig. 4. Binary, multi-class, and multi-label classification.

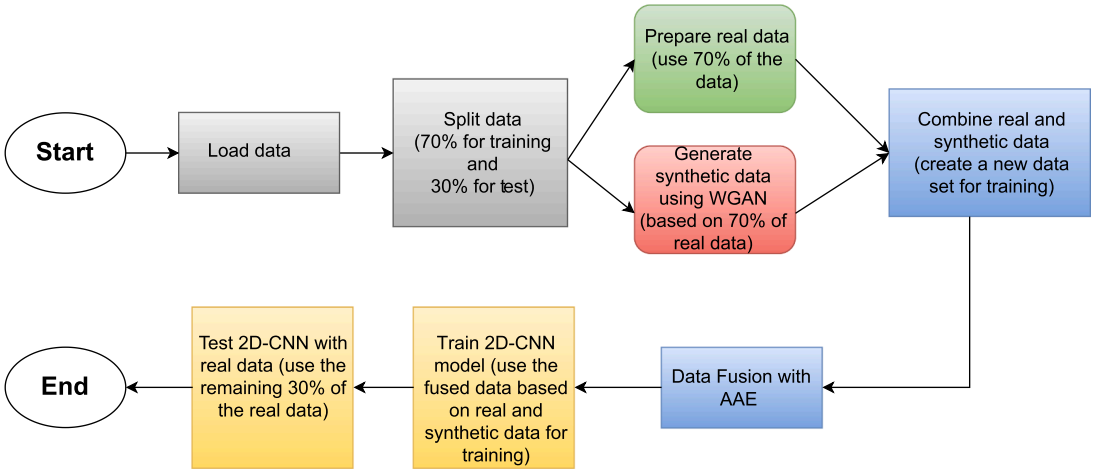

Fig. 5. Proposed methodology framework.

methodology allows us to explore the effectiveness of different sensor combinations, leverage the power of synthetic data for training, and ensure the generalizability of our proposed approach across various data distributions. The combination of individual classifiers and the multi-label class classification strategy, along with the integration of synthetic data and cross-validation, strengthens the validity and applicability of our model in the critical task of leakage detection.

Fig. 5 depicts the overarching flowchart of the proposed methodology designed for the detection of pipeline leaks. The framework integrates WGAN and AAE for the fusion of both synthetic and real data (proposed WGAN-AAE fusion approach), with 2D-CNNs to address the classification challenges in the pipeline anomaly detection process.

3. Experimental system

In the subsequent sections, we elaborate on the design of the experimental setup intended to validate our proposed algorithm for anomaly detection in pipelines.

3.1. Testbed design

To evaluate the proposed framework, a custom-built pipeline testbed was developed using FBG sensors to monitor both operational and structural pipeline parameters. The test setup features a steel pipe measuring 5.95 meters in length, with a nominal diameter of 100 mm and a wall thickness of 5 mm, resulting in an internal volume of approximately 0.2782 m^3. An overview of the complete system configuration is provided in Fig. 6. As illustrated in Fig. 7, the pipeline was outfitted with essential components such as valves and pressure gauges. The pipe material and wall thickness were chosen to allow welding of threadolet required for the secure attachment of fittings. In order to make the pipe easier to handle and portable, it was initially segmented into four parts. The sections were then welded together and secured with M10 bolts and nuts, with flanges welded to both ends. In order to maintain a watertight seal, rubber gaskets were inserted between the flanges. The pipe was incorporated with six radial openings, each performing a specific role. The first two openings were for fluid inlet and outlet, while the remaining four were used to simulate controlled leakages. There was a comprehensive assembly on the inlet side, including a ball valve, a pressure gauge, a flow meter, and a pressure-reducing valve. Single ball valves were installed on the outlet side of the system to regulate the flow. During testing, each leakage simulation point was equipped with a ball valve, which allowed precise control of leak conditions.

Each designated leak point on the pipeline was equipped with an auxiliary ball valve so that leakage events could be replicated at multiple locations along the pipeline. Under controlled leakage flow rates, this setup enabled consistent repetition of tests. The valve mounted directly to the pipe served as an on/off switch, while the secondary

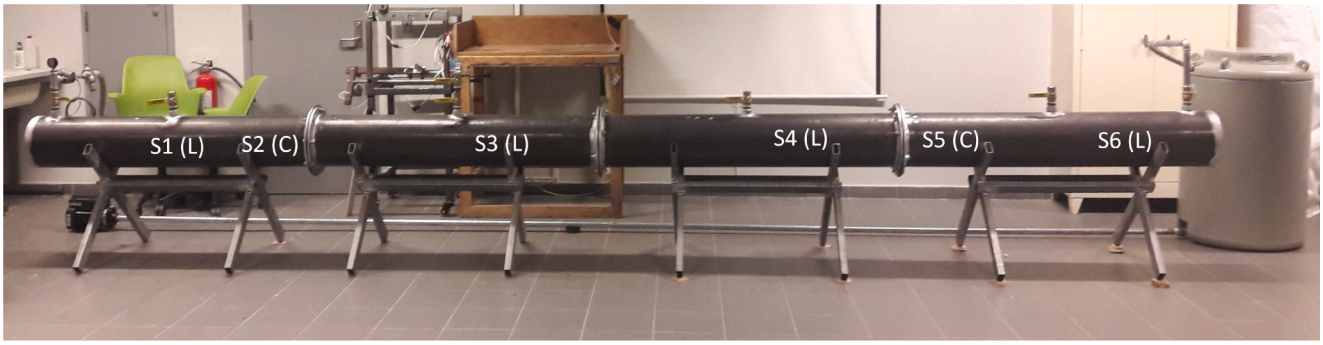

(a)

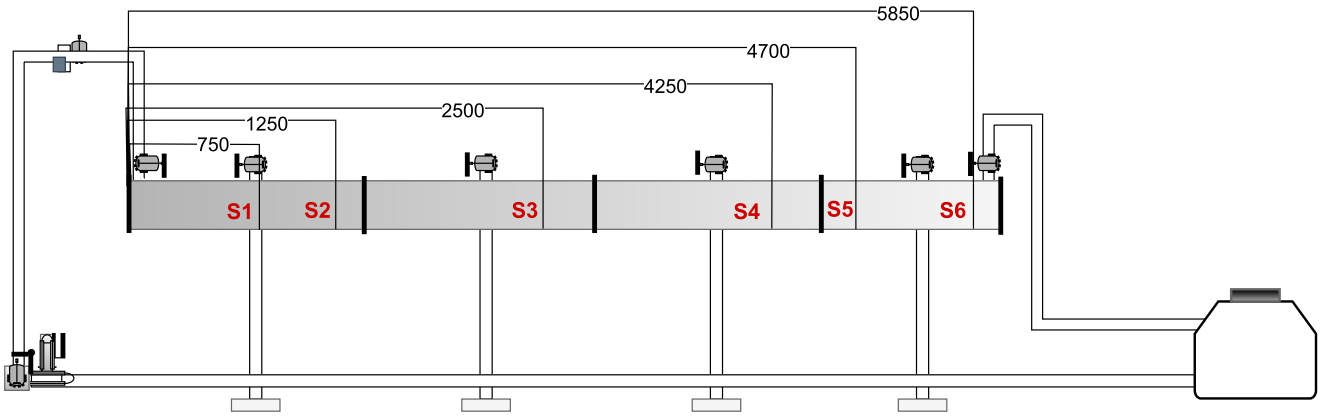

(b)

Fig. 6. Pipeline testbed: (a) experimental setup and (b) dimensions and sensor locations.

valve mounted above enabled partial opening for precise adjustment of leak intensity.

Regarding instrumentation, the setup utilised two types of fiber optic sensors provided by Micron Optics. Longitudinal strain data were obtained using temperature-compensated FBG sensors (model `os3155`), which were spot-welded onto selected locations on the pipe surface. Circumferential strain was measured using optical strain gauges (model `os3100`), adhered to the pipe with epoxy. A total of six FBG sensors, labeled S1 through S6, formed the sensing network. A longitudinal sensor was installed in position S1, a longitudinal sensor in position S3, a longitudinal sensor in position S4, and a circumferential sensor in position S5. Data acquisition was performed using the Micron Optics si255 Hyperion interrogator, operating at a sampling frequency of 1 kHz.

3.2. Test scenarios

Several leakage experiments were conducted by altering pipeline configurations while maintaining standard operating conditions, such as fixed pressure and flow rate. During each test, data was collected over a period of 60 seconds. At the 30-second mark, a leakage event was simulated by opening one of the designated pressure valves. The procedural flow of the experimental testing is illustrated in Fig. 8.

As a result, the collected dataset captures two distinct operational phases: the first 30 seconds reflect normal pipeline behavior under standard conditions, while the latter 30 seconds correspond to simulated leakage occurring under the same operational parameters. Experiments were conducted across three pressure levels (0.6, 0.8, and 1 bar) and three flow rates (10, 15, and 20 GPM (Gallons per minute)). Additionally, four different leakage locations and two leakage magnitudes were tested. Leakage size was controlled via the aperture of the secondary valve, categorized as small (approximately 20 % open) and large (fully open, 100 %). A systematic variation of parameters enriched the dataset and contributed to robust classifier performance across a wide range of leakage conditions. The investigated combinations of these parameters are depicted in Fig. 9. Each combination was tested, with the entire process being repeated 10 times. Consequently, 72 scenarios were tested with 720 cumulative recordings.

3.3. Sensor data

The raw strain signals captured by the interrogation unit exhibited varying degrees of noise, with SNRs ranging between 1.85 and 10.23 depending on the flow conditions and leakage configurations. To improve signal quality, a denoising procedure was carried out in MATLAB. This process began with the application of a 400 ms moving average filter to smooth short-term fluctuations, followed by a low-pass filter with a cutoff threshold of 10^{-5} to further suppress high-frequency noise. After filtering, each sensor signal was zero-centred and cropped to a 15-second interval, effectively removing redundant data outside the region of interest. In a second, representation-level stage, the AAE can act as a learned denoiser during fusion: its bottleneck and adversarial prior matching project inputs onto a compact, domain-aware latent manifold, compressing nuisance variation while preserving leak-salient structure for downstream classification. Fig. 11 displays the raw, unfiltered output from all six sensors (S1-S6) under test conditions involving a 20 GPM flow rate, 1 bar pressure, a large leakage, and location L1. The corresponding denoised sensor responses for the same setup are shown in Fig. 12.

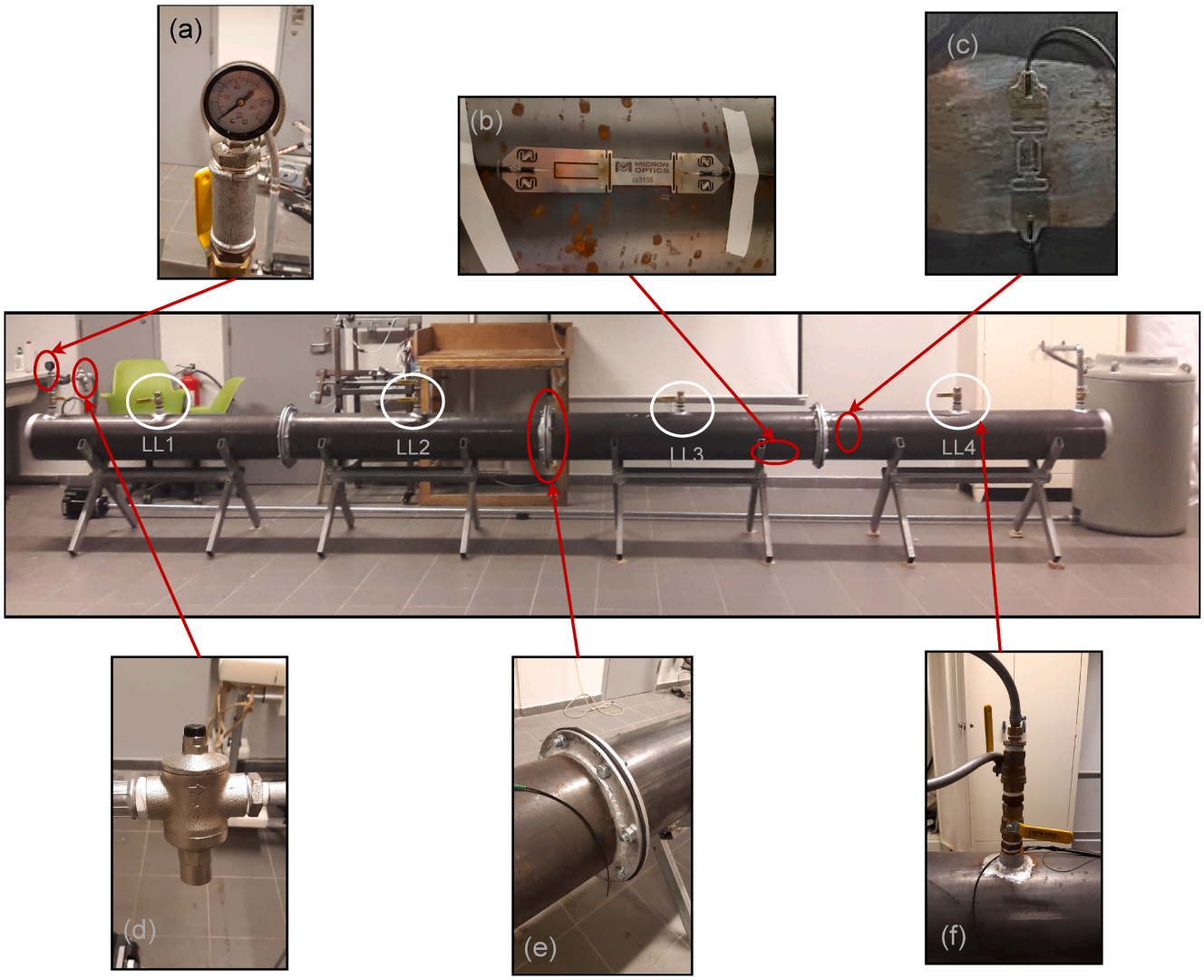

Fig. 7. Components of the experimental pipeline: (a) inlet pressure gauge, (b) longitudinally mounted Fiber Bragg Grating (FBG) temperature-compensated strain sensor, (c) circumferentially mounted FBG strain sensor, (d) pressure regulating valve, (e) flange of the pipe, and (f) leakage valve assembly.

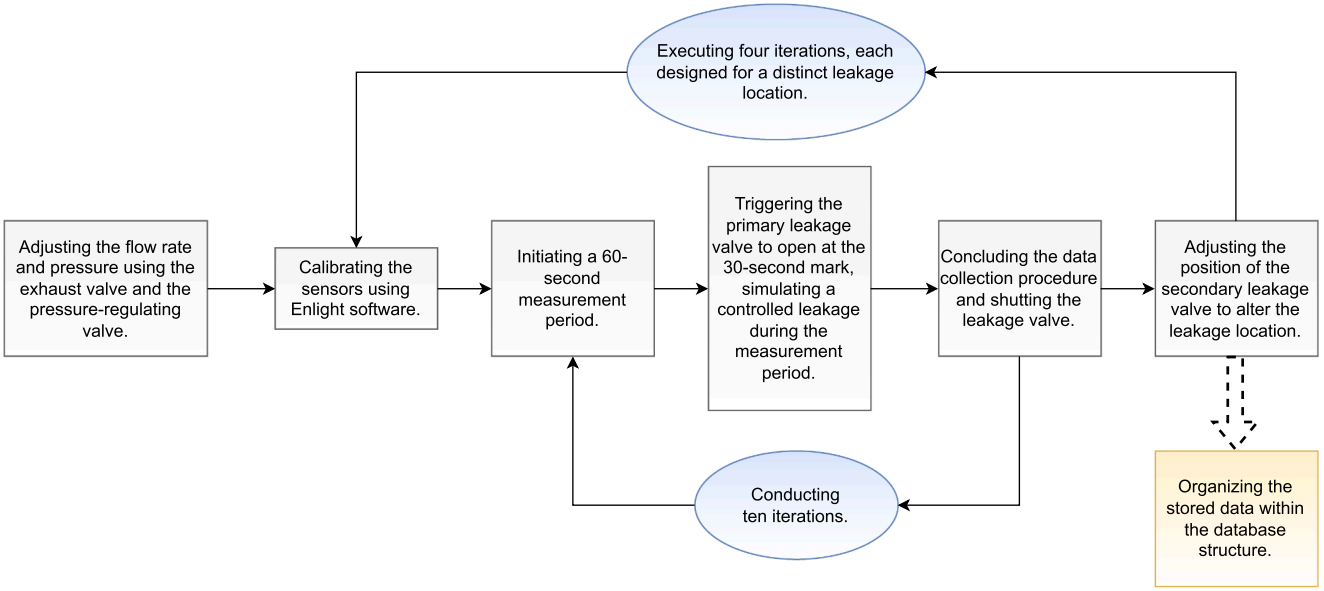

Fig. 8. Flow diagram of the experimental procedure.

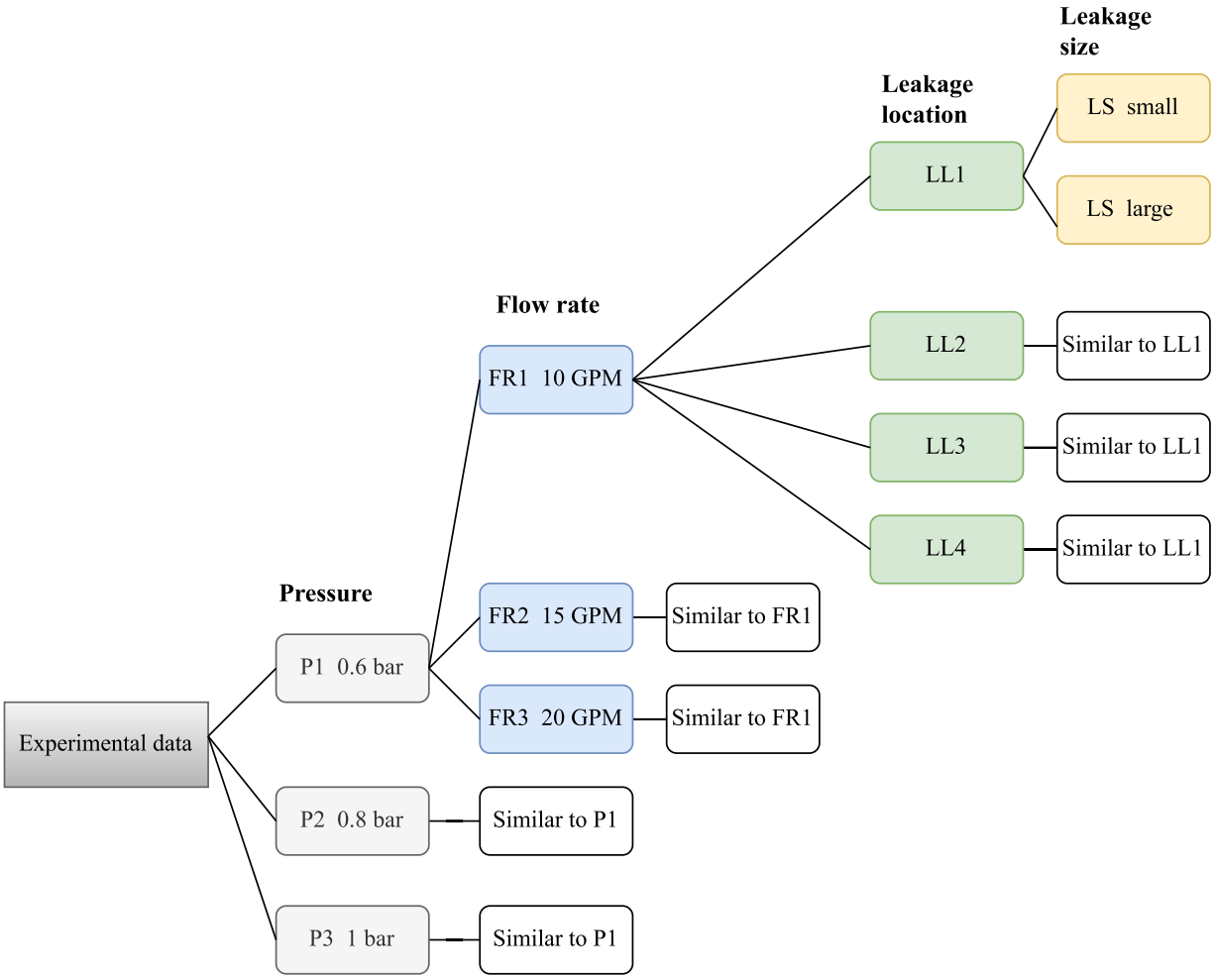

Fig. 9. Investigated test cases (P represents pressure, FR stands for flow rate, LL indicates the location of leakage, and LS denotes the size of the leakage).

The surface strain variations observed in this study can be compared with findings from earlier investigations. For example, Jiang et al. [53] reported surface strain changes of approximately 5-6 με under a pressure of 120 kPa (1.2 bar), while Jia et al. [54] recorded strain variations of 90-120 με at a significantly higher pressure of 1.2 MPa (12 bar). Notably, these tests were performed on pipes with similar characteristics to the one used in this study.

It is important to highlight that oil transmission pipelines generally operate at much higher internal pressures than those simulated in our experimental setup [55], resulting in greater hoop stress. Because of the increased amplitude of the NPW, these elevated pressures are expected to amplify the strain response under leakage conditions, leading to a higher SNR and more clearly defined strain drop signatures.

Fig. 10 provides a comprehensive overview of both the experimental and analytic phases in our proposed approach for assessing pipe condition. The diagram illustrates the sequential steps, starting with the installation of various FBG sensors in different directions and locations. Data are denoised, followed by synthetic data generation and fusion of real and synthetic data using the WGAN-AAE fusion approach, creating informative features while reducing dimensionality. Using combined real and synthetic data, the proposed 2D-CNN architecture is then trained and tested on real data, followed by a 10-fold cross-validation process. A total of 10 iterations is performed with WGAN to generate data. Multiple classifiers are used to address the problem, including a simple classifier for flow rate, pressure, leak size, and leak location, as well as a multi-label class classification approach.

4. Parameter impact analysis

Following is a detailed analysis of how pressure, flow rate, leakage size, and leakage location affect strain data captured by the sensors. In order to determine the specific impact of each parameter on the measured signals, each parameter was examined independently.

4.1. Impact of flow rate

Flow rate was analyzed in four different testing scenarios with varying flow rates in order to evaluate how it impacted the strain data recorded. Several parameters, including the location and size of the leakage hole, can also alter the observed effects of flow rate variations in these scenarios.

At the first test scenario, measurements were taken at 0.8 psi with a small leakage size at location L1, closest to the inlet valve and relevant sensors. As shown in Fig. 13, an increase in flow rate leads to a noticeable reduction in the measured strain. This trend was detected by both the longitudinal and circumferential sensors. Specifically, the longitudinal sensor recorded a strain difference of 0.25 $\mu\epsilon$ between 10 GPM and 20 GPM and 0.05 $\mu\epsilon$ between 15 GPM and 20 GPM. The circumferential sensor exhibited a more pronounced response, with a difference of 0.45 $\mu\epsilon$ between 10 GPM and 20 GPM and 0.1 $\mu\epsilon$ between 15 GPM and 20 GPM. These results emphasize the sensitivity of both sensor types to variations in flow rate under this configuration.

In the second scenario, the pressure remained constant at 0.8 bar, but the leakage location was changed to L4, the point furthest from the

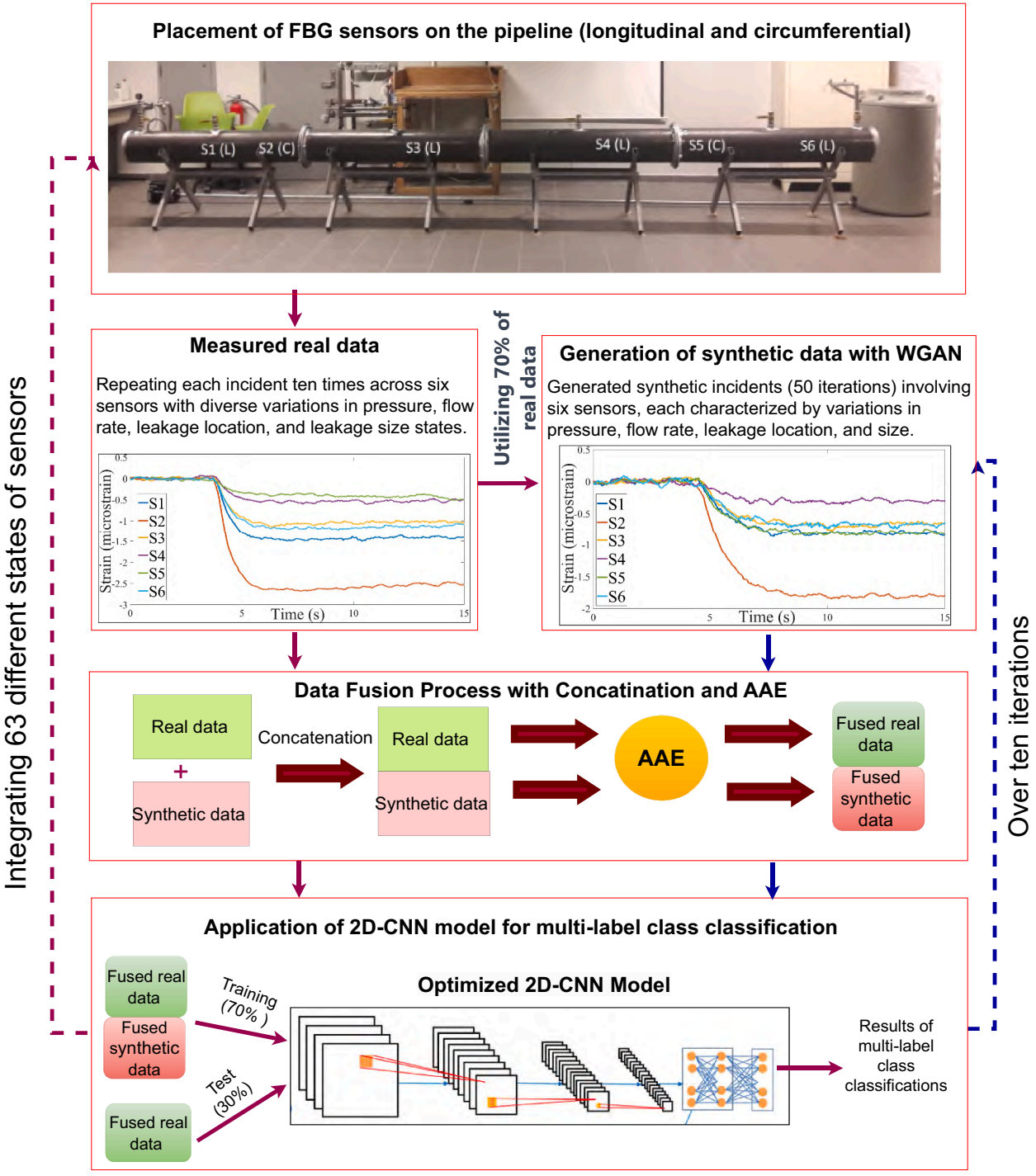

Fig. 10. Comprehensive overview of the experimental and analytic phases of the proposed pipeline evaluation framework.

inlet. As depicted in Fig. 14, increasing the flow rate again resulted in a reduction in strain. The longitudinal sensor showed a difference of 0.12 $\mu\epsilon$ between 10 GPM and 20 GPM and 0.23 $\mu\epsilon$ between 15 GPM and 20 GPM. The circumferential sensor, on the other hand, exhibited consistent changes of 0.31 $\mu\epsilon$ between both 10 GPM and 20 GPM and 15 GPM and 20 GPM. In contrast, these findings highlight the differences between the sensitivities and responses of the two sensor orientations at different leakage positions.

As the leakage size increases, the third scenario replicates the conditions of the first. Test conditions were conducted at 0.8 bar pressure with a large leak located at L1. Comparing this setup to the initial scenario offers valuable insights into how leakage size affects the strain response. As depicted in Fig. 15, changes in flow rate produce a more significant impact on strain when a larger leak is present. The longitudinal sensor recorded a difference of 0.21 $\mu\epsilon$ between 10 GPM and 20 GPM and 0.05 $\mu\epsilon$ between 15 GPM and 20 GPM. Meanwhile, the circumferential sensor showed a difference of 0.39 $\mu\epsilon$ between 10 GPM and 20 GPM and 0.09 $\mu\epsilon$ between 15 GPM and 20 GPM. According to these results, strain sensitivity is amplified with increasing leakage size.

In the fourth scenario, the pressure remained at 0.8 bar, but the leakage occurred at location L4 with a large opening. This test aimed to determine whether the distance of the leakage from the sensor affects

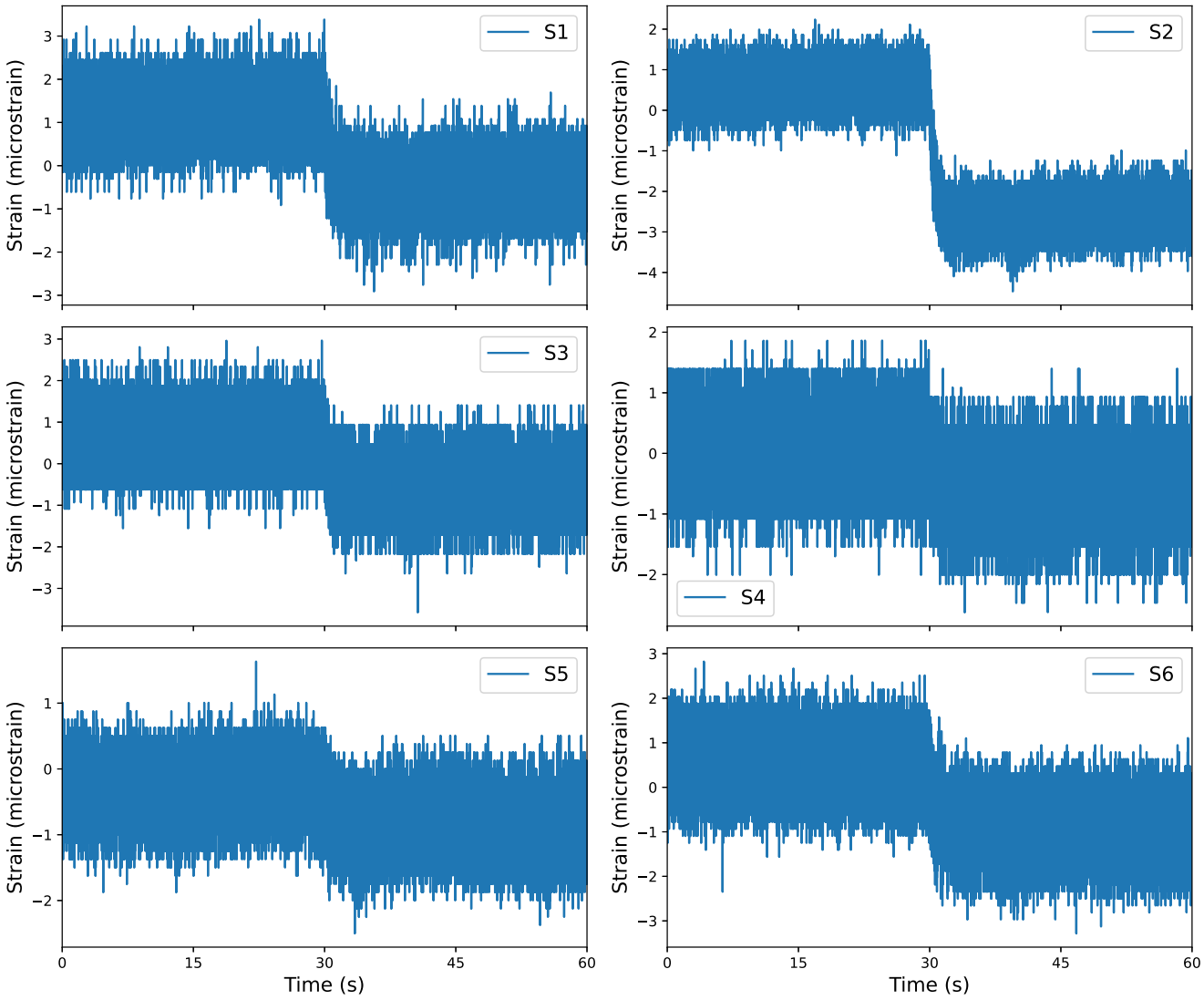

Fig. 11. Raw strain data for all sensors under conditions of flow rate: 20 GPM, pressure: 1 bar, leakage size: large, and leakage location: L1.

strain behaviour under severe leakage conditions. Fig. 16 illustrates the influence of increasing flow rates on measured strain for a large leak located farther from the sensing region. The longitudinal sensor showed a change of 0.27 $\mu\epsilon$ between 10 GPM and 20 GPM and 0.10 $\mu\epsilon$ between 15 GPM and 20 GPM. The circumferential sensor exhibited a more substantial difference-0.49 $\mu\epsilon$ between 10 GPM and 20 GPM, and 0.18 $\mu\epsilon$ between 15 GPM and 20 GPM. These findings show that the sensors respond in a detailed and flow-dependent manner when leakage occurs at more distant locations under larger leak conditions.

Table 3 demonstrates patterns similar to those identified in the earlier scenario, implying that factors such as leakage location, size, flow rate, and sensor type exert limited influence on the overall strain amplitude. A notable difference emerges between the outputs of longitudinal and circumferential sensors, especially in the third case. When compared to scenarios involving smaller leak sizes, this contrast reveals a significant decrease in strain. A similar pattern occurs when a large leak is situated farther from the inlet, where strain is further reduced. It is evident from these results that remote, large-scale leakages have a profound effect on both sensor types and that the system remains responsive to changes in leakage characteristics and positioning.

Table 3
Strain values ($\mu\epsilon$) of different flow rate.

Flow Rate (GPM)	10	15	20
Pressure 0.8 bar, leakage location L1, small leak size			
Longitudinal	-1.70	-1.5	-1.45
Circumferential	-3.1	-2.75	-2.65
Pressure 0.8 bar, leakage location L4, small leak size			
Longitudinal	-1.61	-1.72	-1.49
Circumferential	-2.83	-3	-2.69
Pressure 0.8 bar, leakage location L1, large leak size			
Longitudinal	-1.11	-0.95	-0.9
Circumferential	-2.30	-2	-1.91
Pressure 0.8 bar, leakage location L4, large leak size			
Longitudinal	-1.12	-0.95	-0.85
Circumferential	-2.31	-2	-1.82

4.2. Influence of pressure

To evaluate the influence of pressure on the recorded strain responses, strain measurements were analyzed across three pressure lev-

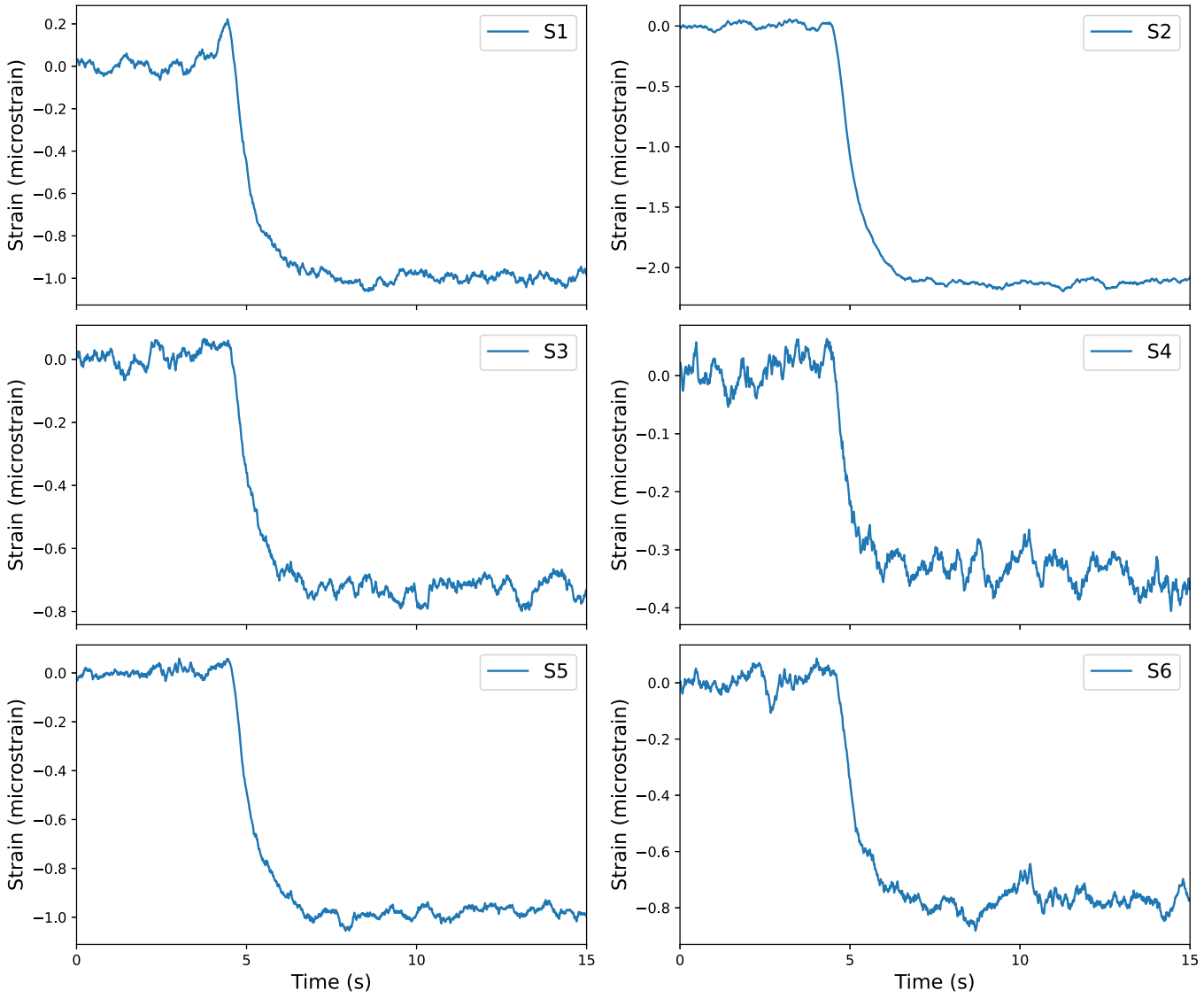

Fig. 12. Denoised strain data for all sensors under conditions of flow rate: 20 GPM, pressure: 1 bar, leakage size: large, and leakage location: L1.

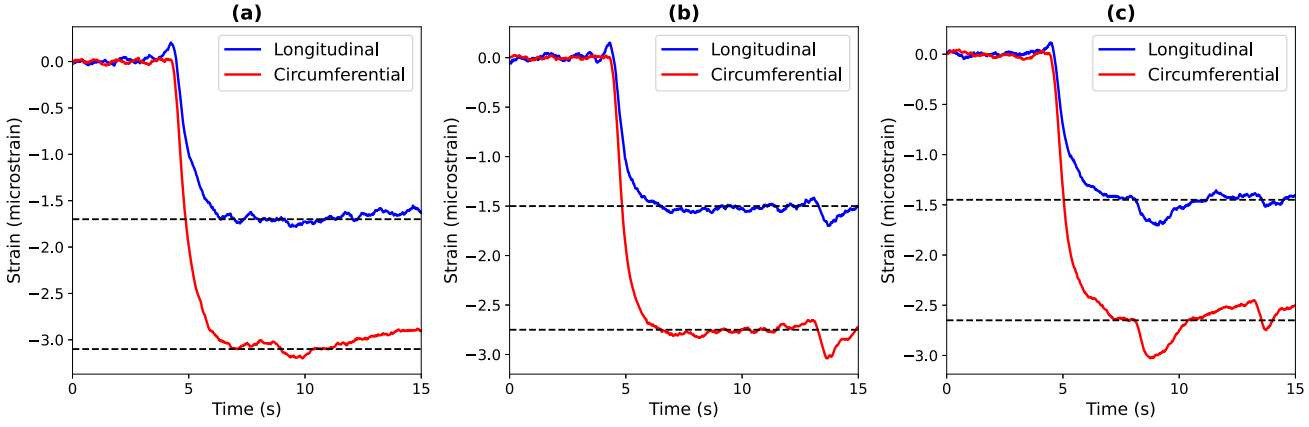

Fig. 13. Comparisons of flow rates at leakage location L1 with a small leakage size, specifically at (a) 10, (b) 15, and (c) 20 GPM under 0.8 bar pressure.

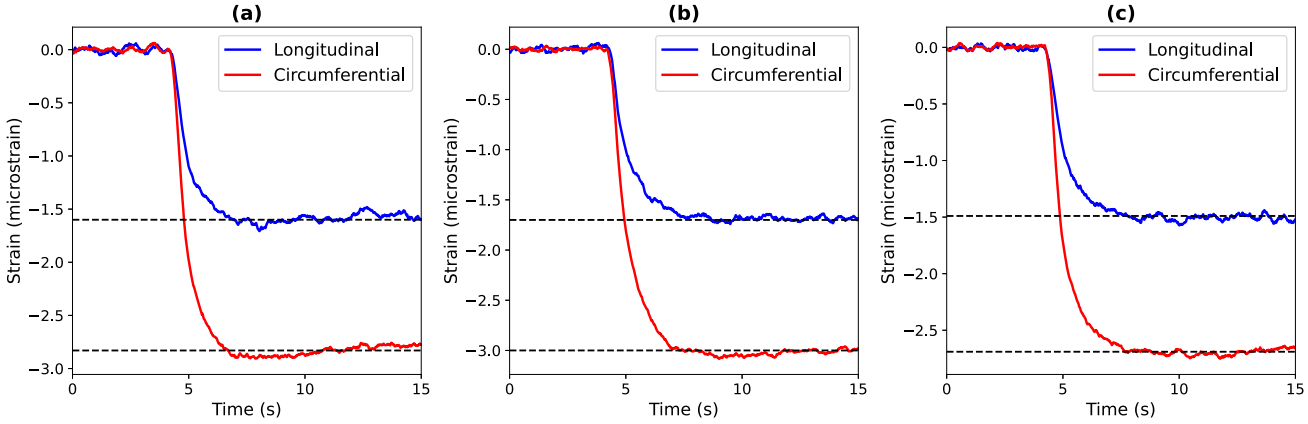

Fig. 14. Comparisons of flow rates at leakage location L4 with a small leakage size, specifically at (a) 10, (b) 15, and (c) 20 GPM under 0.8 bar pressure.

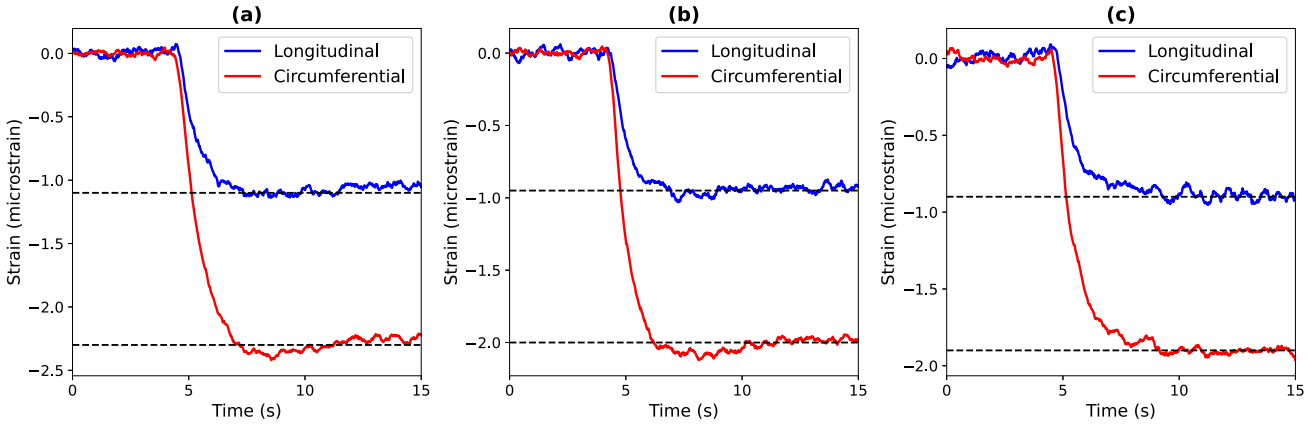

Fig. 15. Comparisons of flow rates at leakage location L1 with a large leakage size, specifically at (a) 10, (b) 15, and (c) 20 GPM under 0.8 bar pressure.

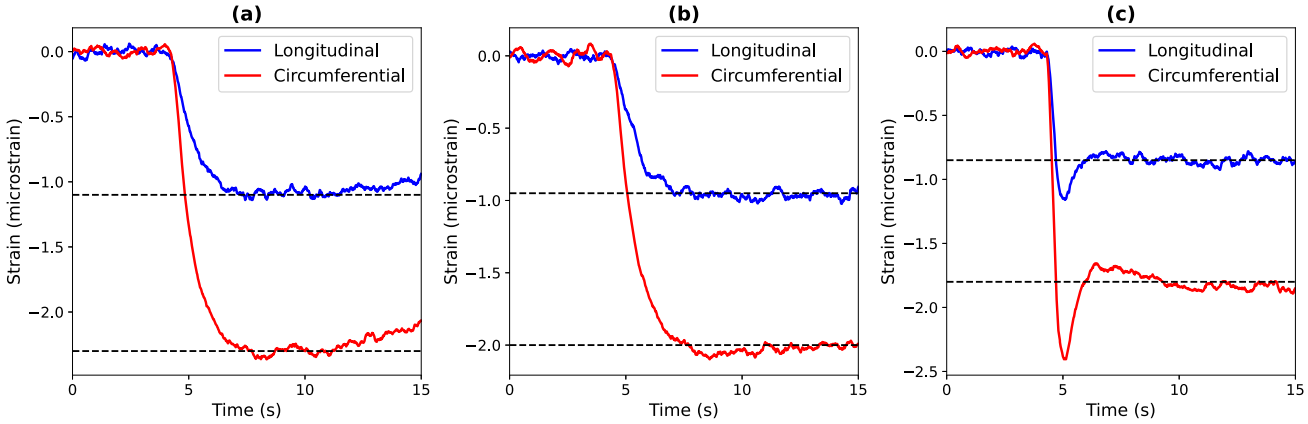

Fig. 16. Comparisons of flow rates at leakage location L4 with a large leakage size, specifically at (a) 10, (b) 15, and (c) 20 GPM under 0.8 bar pressure.

els within four distinct experimental scenarios. These scenarios facilitate a comparative assessment of how pressure variations affect strain under different combinations of flow rates, leakage sizes, and leakage locations.

The first scenario explores the effect of pressure changes when a small leakage occurs near the sensors at location L1. A key observation is the contrast between the influence of pressure and flow rate: while increasing the flow rate results in a modest decrease in strain, higher pressure levels lead to a more substantial drop. As illustrated in Fig. 17, strain measurements decline with rising pressure. The longitudinal sensor shows a reduction from $-1.35\ \mu\epsilon$ at 0.6 bar to $-2.05\ \mu\epsilon$ at 1 bar, while the circumferential sensor exhibits a corresponding decrease from $-2.40\ \mu\epsilon$to $-3.75\ \mu\epsilon$. The net differences between 0.6 bar and 1 bar are $0.70\ \mu\epsilon$ and $1.35\ \mu\epsilon$ for the longitudinal and circumferential sensors, respectively.

In the second scenario, data were collected at a constant flow rate of 15 GPM, with a small leakage introduced at location L4, situated farther from the sensor array. In this case, pressure still impacts the measured strain, although the effect appears to be slightly less pronounced compared to when the leak is located near the sensors (see Fig. 18). The

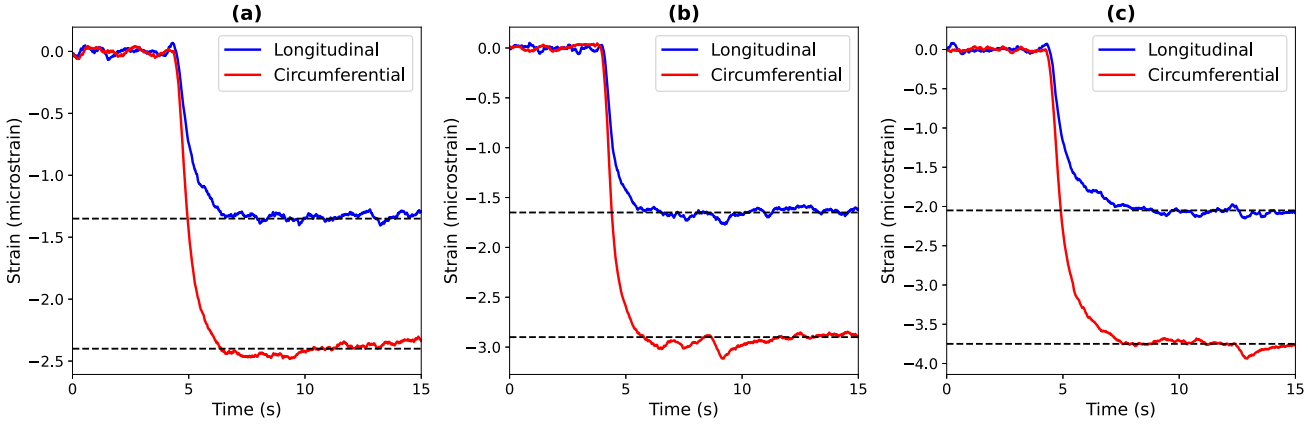

Fig. 17. Comparison of strain at leakage location L1 with a small leakage size under a flow rate of 15 GPM for pressures of (a) 0.6, (b) 0.8, and (c) 1 bar.

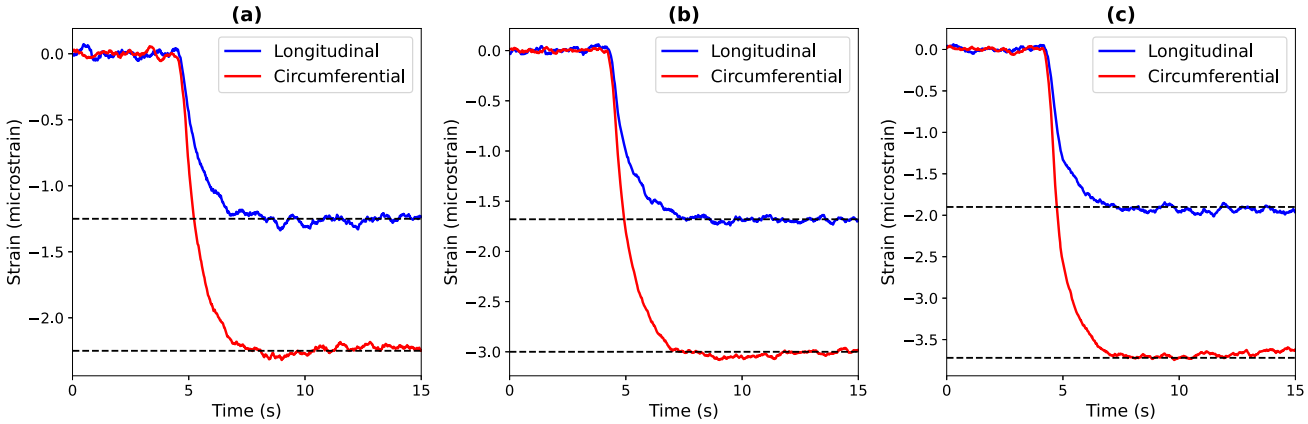

Fig. 18. Comparison of strain at leakage location L4 with a small leakage size under a flow rate of 15 GPM for pressures of (a) 0.6, (b) 0.8, and (c) 1 bar.

longitudinal sensor reading decreases from −1.25 at 0.6 bar to −1.90 at 1 bar, and the circumferential sensor drops from −2.25 to −3.72. This results in differences of 0.65 $\mu\epsilon$ and 1.47 $\mu\epsilon$ for the longitudinal and circumferential sensors, respectively, between the lowest and highest pressure levels.

The third scenario considers measurements taken at a flow rate of 15 GPM with a large leakage size positioned at location L1. This setup enables a comparison with the first scenario to assess the influence of leakage size on strain behavior. As illustrated in Fig. 19, a larger leakage results in a more pronounced strain drop than a smaller leak. Additionally, the sensitivity of the strain response to pressure increases with larger leakage sizes. The longitudinal sensor reading decreases from −0.80 $\mu\epsilon$ at 0.6 bar to −1.10 $\mu\epsilon$ at 1 bar, while the circumferential sensor drops from −1.65 $\mu\epsilon$ to −2.30 $\mu\epsilon$ over the same pressure range. The resulting differences are 0.30 $\mu\epsilon$ for the longitudinal sensor and 0.65 $\mu\epsilon$ for the circumferential sensor.

The fourth scenario, shown in Fig. 20, involves a similar configuration, with a large leakage occurring at the more distant location L4 and the flow rate maintained at 15 GPM. Interestingly, the measured strain values under these conditions closely match those observed in the third scenario, where the leak was located near the sensors. The longitudinal sensor drops from −0.82 $\mu\epsilon$ at 0.6 bar to −1.10 $\mu\epsilon$ at 1 bar, while the circumferential sensor decreases from −1.80 $\mu\epsilon$ to −2.301 $\mu\epsilon$. The observed differences are 0.28 $\mu\epsilon$ and 0.521 $\mu\epsilon$ for the longitudinal and circumferential sensors, respectively. Based on these results, leakage location has a less significant impact on pressure sensitivity for large leaks.

The effects are outlined in Table 4, revealing the resemblance between the recorded values for the first two scenarios.

Table 4
Strain values ($\mu\epsilon$) were recorded for different pressure variation scenarios at 15 GPM.

Pressure (bar)	0.6	0.8	1
Flow rate 15 GPM, Leakage location L1, small leak size			
Longitudinal	-1.35	-1.65	-2.05
Circumferential	-2.40	-2.90	-3.75
Flow rate 15 GPM, Leakage location L4, small leak size			
Longitudinal	-1.25	-1.68	-1.90
Circumferential	-2.25	-3	-3.72
Flow rate 15 GPM, Leakage location L1, large leak size			
Longitudinal	-0.80	-0.95	-1.10
Circumferential	-1.65	-2.00	-2.30
Flow rate 15 GPM, Leakage location L4, large leak size			
Longitudinal	-0.82	-0.95	-1.10
Circumferential	-1.80	-2.08	-2.301

4.3. Effect of leakage size

The smallest strain drop is observed when the pipe flow is characterized by low pressure and a high flow rate, as deduced from the variations in pressure and flow rate. Conversely, the largest strain drop occurs in the opposite configuration. Using these contrasting scenarios to analyze the strain measurements across different leakage sizes can provide valuable insight into the impact of leakage size.

As illustrated in Fig. 21, the strain drop disparity between a substantial and a minor leakage is above 70 % when assessing maximal drops

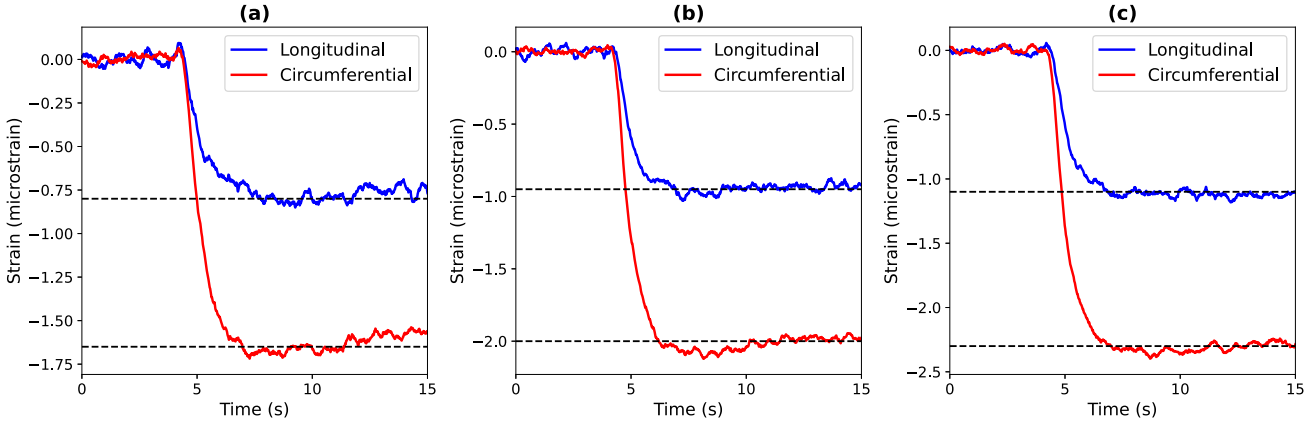

Fig. 19. Comparison of strain at leakage location L1 with a large leakage size under a flow rate of 15 GPM for pressures of (a) 0.6, (b) 0.8, and (c) 1 bar.

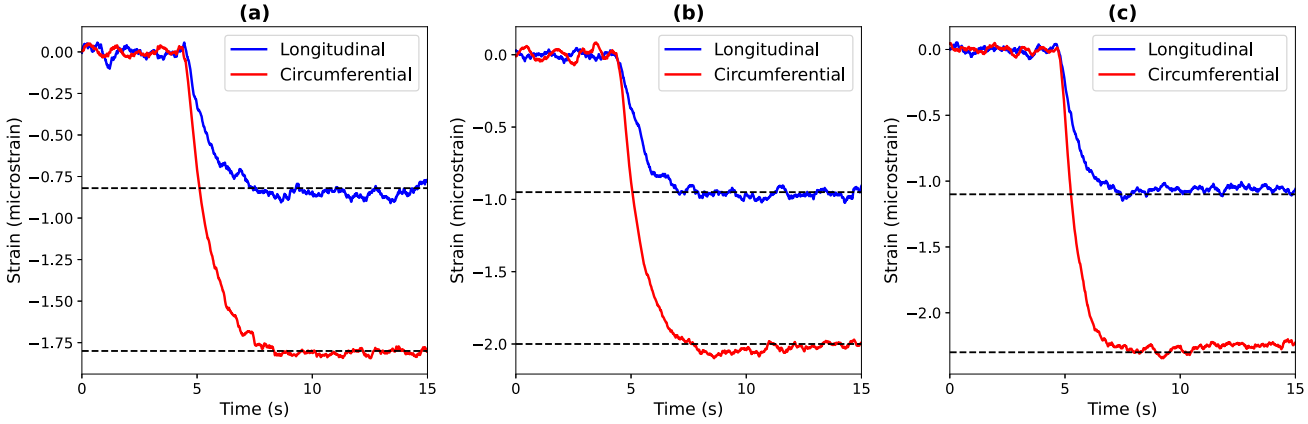

Fig. 20. Comparison of strain at leakage location L4 with a large leakage size under a flow rate of 15 GPM for pressures of (a) 0.6, (b) 0.8, and (c) 1 bar.

(a and c) and 40 % for minimal drops (b and d) using longitudinal sensors. In contrast, circumferential sensors exhibit above 50 % alteration in both situations. This discovery suggests that longitudinal sensors might display greater sensitivity to variations in leakage size compared to circumferential sensors. In the first scenario, for the longitudinal sensor, the strain values are -1.45 $\mu\epsilon$ and -1.77 $\mu\epsilon$ for large and small leaks, respectively. Simultaneously, the circumferential sensor records strain values of -2.60 $\mu\epsilon$ and -3.30 $\mu\epsilon$ for large and small leaks, revealing the influence of leak size on strain measurements. For the second scenario, the longitudinal sensor reports strain values of -0.98 $\mu\epsilon$ and -1.00 $\mu\epsilon$ for large and small leaks, respectively. Correspondingly, the circumferential sensor records strain values of -2.00 $\mu\epsilon$ and -2.25 $\mu\epsilon$ for large and small leaks, reaffirming the impact of both leak size and sensor direction on strain measurements.

Table 5 delineates strain values recorded for various pressure scenarios at two scenarios.

Table 5
Strain values ($\mu\epsilon$) were recorded for different pressure variation scenarios at 15 GPM.

Leak size	Large	Small
Flow rate 10 GPM, Pressure 0.6 bar, Leakage location L1		
Longitudinal	-1.45	-1.77
Circumferential	-2.60	-3.30
Flow rate 20 GPM, Pressure 1 bar, Leakage location L4		
Longitudinal	-0.98	-1
Circumferential	-2.00	-2.25

4.4. Influence of leakage location

While the magnitude of the strain drop remains unaffected by the location of the leakage, it does influence the shape of the strain curve. To examine this impact, the location of the leakage was altered in various scenarios–specifically, those producing the largest and smallest strain drops with both large and small leakage sizes. The most noticeable distinction in the signals resulting from changes in leakage location was observed in the gap between the intercepts of sensors 1 and 2, using sensor10ı́s final steady-state strain value (see Fig. 22). Strain values are presented for each leakage location, differentiating between the measurements obtained from the longitudinal and circumferential sensors. For instance, at leak location L1, the longitudinal sensor records a strain value of -1.17 $\mu\epsilon$, while the circumferential sensor registers a corresponding value of -2.53 $\mu\epsilon$. This pattern continues for leak locations L2, L3, and L4, with distinct strain values captured by both sensor orientations. The corresponding data is outlined in Table 6.

5. Data analysis and results

The section outlines the data analysis procedures, including WGAN-based synthetic data generation, AAE-based data fusion, and 2D-CNN-

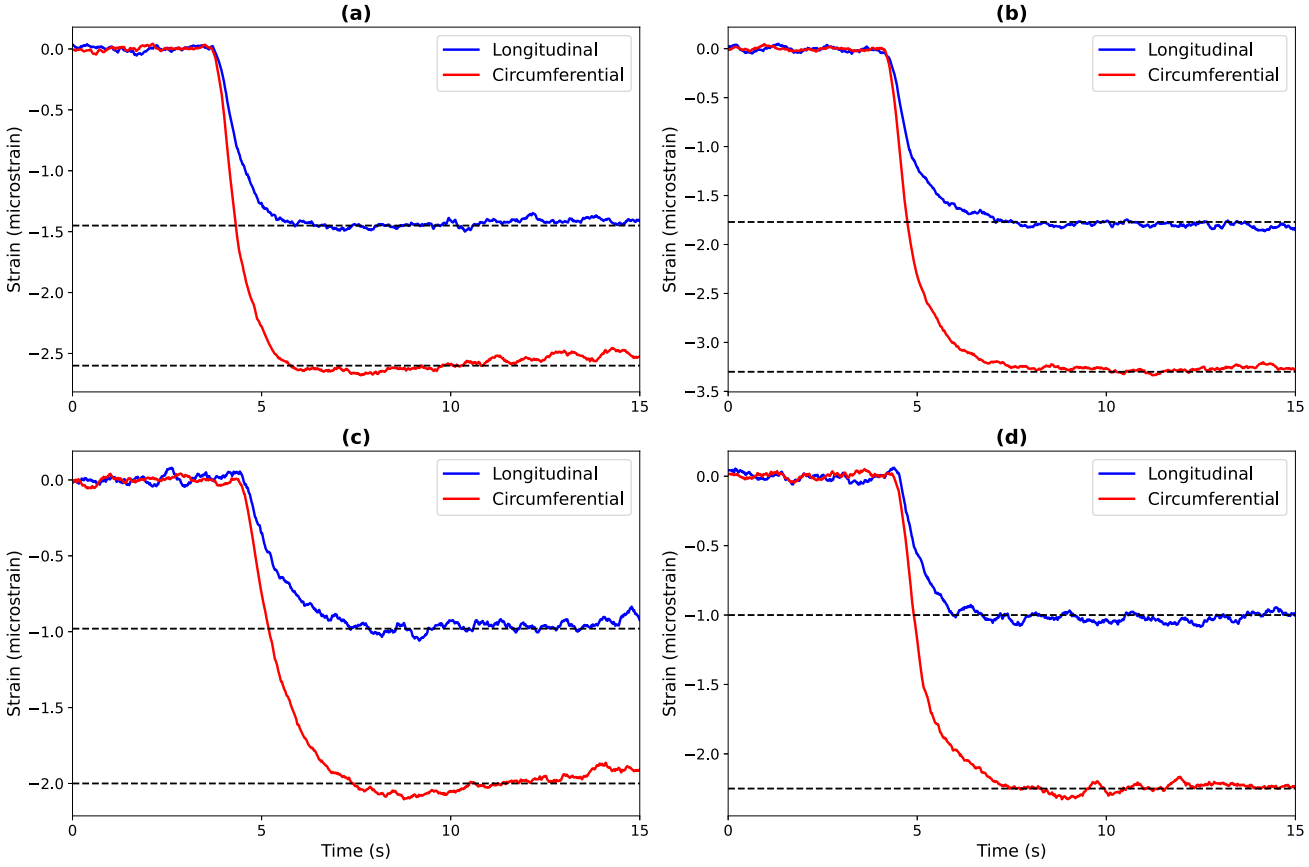

Fig. 21. Strain measurements for both the largest and smallest drop cases are recorded in instances of both small leakage (a and b) and large leakage (c and d).

Table 6
Strain values ($\mu\epsilon$) for different leakage locations.

Leak location	L1	L2	L3	L4
Flow rate 10 GPM, Pressure 1 bar, Large Leakage				
Longitudinal	-1.17	-1.21	-1.12	-1.21
Circumferential	-2.53	-2.68	-2.42	-2.65

based classification. In addition, the results of the classification are presented and discussed in detail.

5.1. Generation of synergic data using WGAN

In this section, we delve into the utilisation of synthetic data generated through the WGAN for the training of the 2D-CNN model. The synthetic dataset is crafted by blending 70 % real data with the generated samples over 10 training iterations. This iterative process aims to refine and enhance the quality of the generated data. To achieve a more robust and representative final set of synthetic data, we employ a consideration of the mean of the final accuracy across the iterations. This strategic approach not only ensures a convergence towards meaningful synthetic representations but also contributes to the overall effectiveness of the 2D-CNN model during training and subsequent performance evaluation. Fig. 23 displays the real and synthetic strain data from both longitudinal and circumferential sensors in a scenario characterized by a flow rate of 10 GPM, a pressure of 1 bar, and a significant leakage at location 1.

Fig. 24 presents a comprehensive evaluation of the WGAN performance through four sub-figures (S3):

- (a) The top-left subfigure tracks the discriminator and generator loss over the training epochs for the WGAN. Both the discriminator and generator losses tend towards zero, indicating that the discriminator becomes increasingly incapable of distinguishing between real and synthetic samples, while the generator effectively minimises its loss, generating samples that closely resemble real data.
- (b) The top-right subfigure depicts the Wasserstein loss on both real and synthetic samples. The trend here is a gradual reduction in Wasserstein loss for both real and synthetic samples, approaching zero. This suggests that the WGAN is successfully minimising the dissimilarity between the true and generated data distributions, leading to high-quality synthetic samples.
- (c) The bottom-left subfigure visually compares the distributions of real and synthetic samples. Notably, the synthetic distribution closely mirrors a bell curve, indicating that the generator has effectively learned to produce samples that align with the characteristics of the real data distribution. This visual similarity signifies the success of the WGAN in capturing and reproducing the underlying data distribution.
- (d) The bottom-right subfigure employs a boxplot to showcase the Wasserstein losses for both real and synthetic samples. The boxplot for synthetic samples has a larger spread, indicating a greater variability in the Wasserstein losses. This suggests that the generator might face challenges in certain regions of the data space, leading to higher losses for specific generated samples. In contrast, the boxplot for real samples is relatively tighter, indicating more consistent Wasserstein losses for real data, reinforcing the WGAN's ability to generate realistic synthetic data.

Fig. 25 also illustrates the discriminator and generator loss for two representative sensor combinations; in both cases the losses stabilize near zero, indicating robust WGAN training. Other sensor combina-

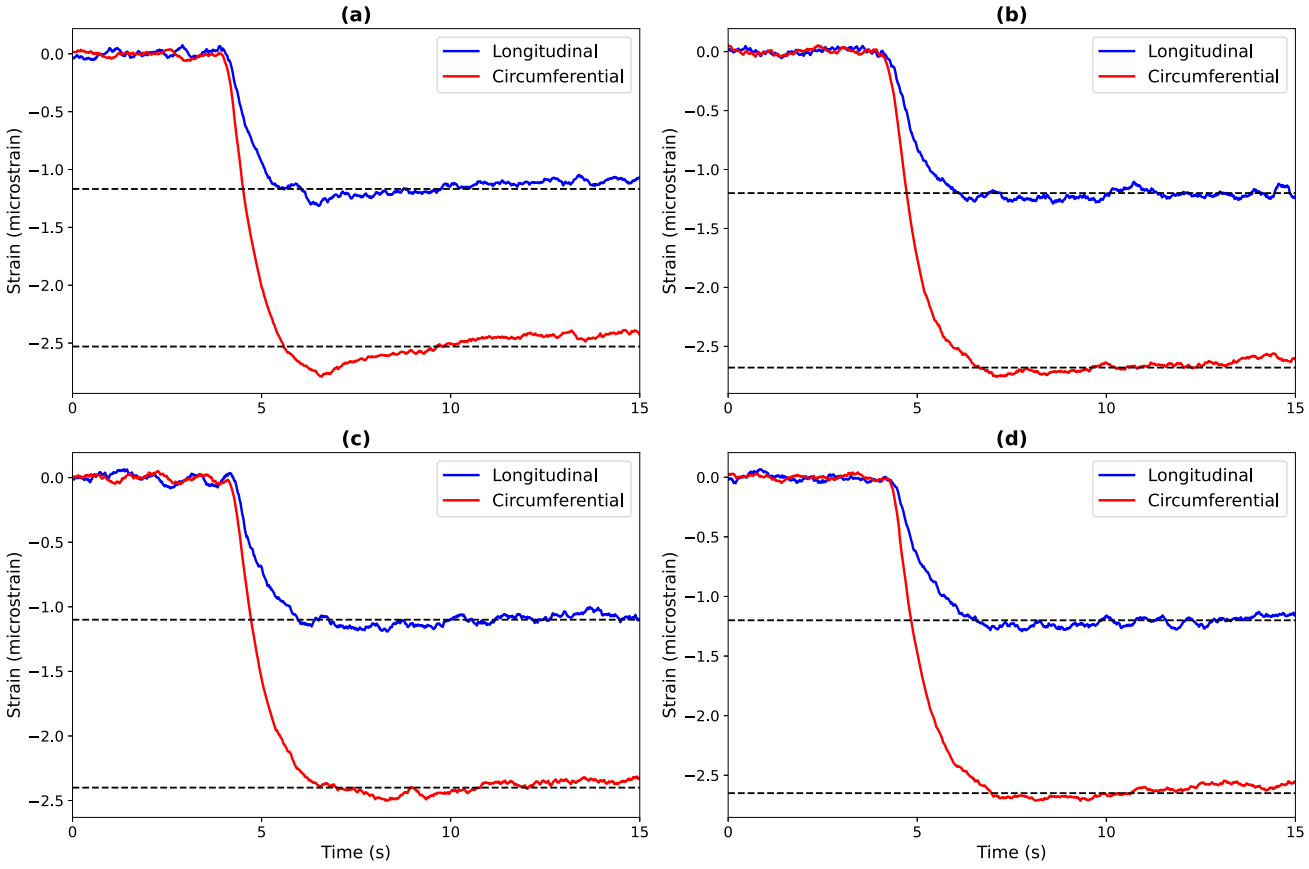

Fig. 22. Comparison of strain at leakage locations (a) L1, (b) L2, (c) L3, and (d) L4 under 1 bar pressure, 10 GPM flow rate, and large leakage size.

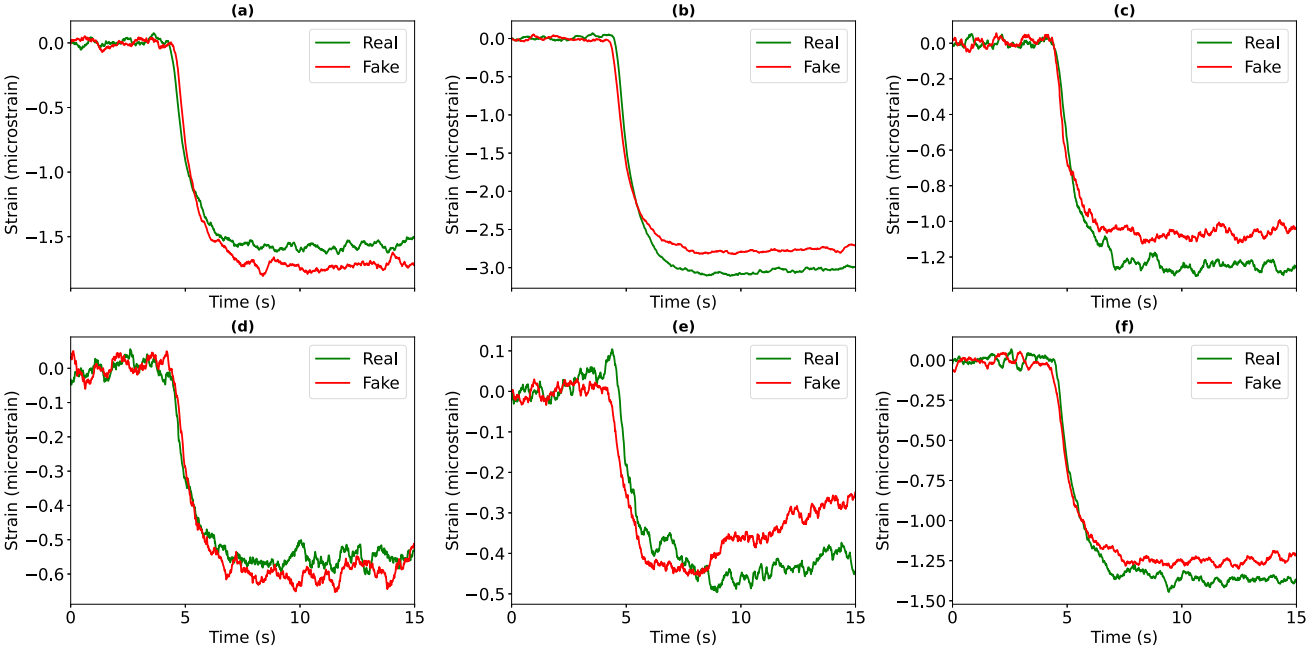

Fig. 23. Real and synthetic strain data for longitudinal and circumferential sensors: (a) S1, (b) S2, (c) S3, (d) S4, (e) S5, and (f) S6 in a scenario with a flow rate of 10 GPM, a pressure of 1 bar, and a substantial leakage at location 1.

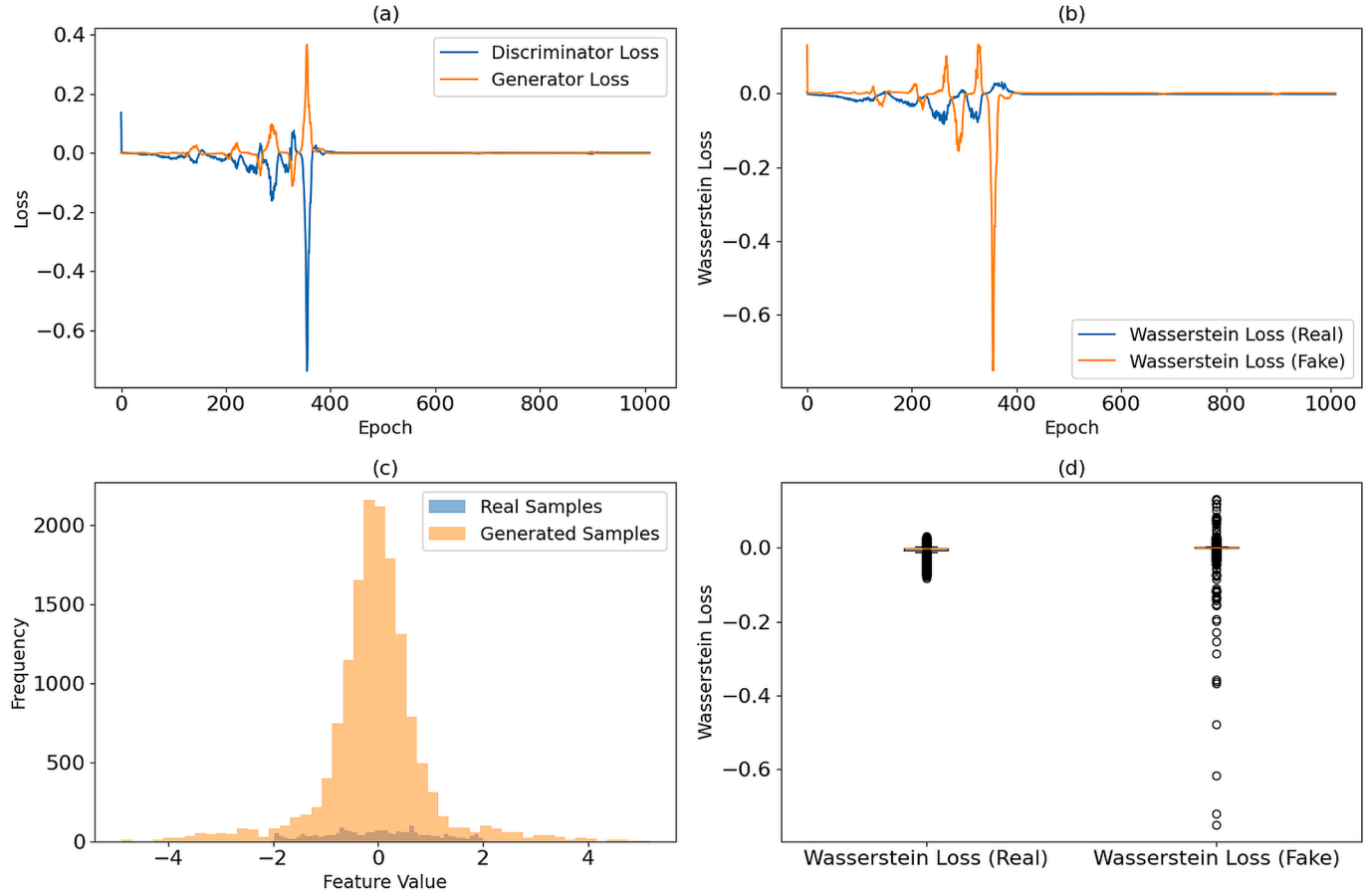

Fig. 24. Performance evaluation of WGAN ((a) Discriminator and generator loss plot, (b) Wasserstein loss on real and synthetic samples plot, (c) Distribution comparison plot (real vs. synthetic), and (d) Wasserstein loss on real vs. synthetic samples boxplot).

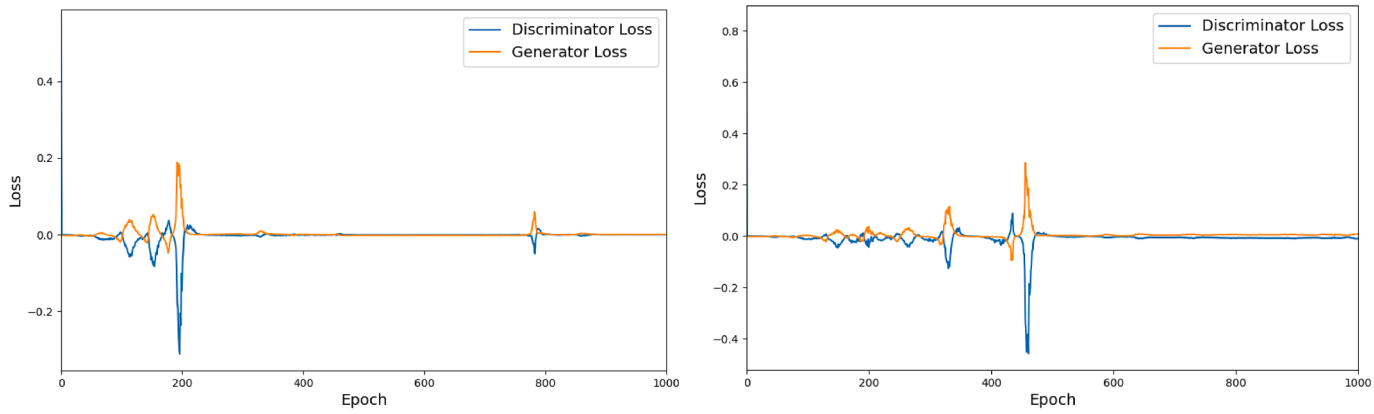

(a) S1 (b) S6

Fig. 25. Discriminator and generator loss across the sensor combinations.

tions exhibit the same convergence pattern, so we report these two as exemplars.

In Fig. 26, the Wasserstein loss plots for two representative sensor combinations are presented. The sub-figures reveal a convergence of loss values toward zero, indicating the effective performance of WGAN in generating synthetic data. Other combinations show the same behavior, so we report these two as exemplars.

5.2. Data fusion with the WGAN-AAE approach

This section delves into the integration of data using WGAN-AAE to extract informative and condensed features, ultimately reducing them to 300 points. Generally, AAE plays a crucial role in this fusion process by leveraging its ability to learn a compact and meaningful representation of the input data. By incorporating adversarial training, the AAE ensures that the generated features capture the essence of the underlying pat-

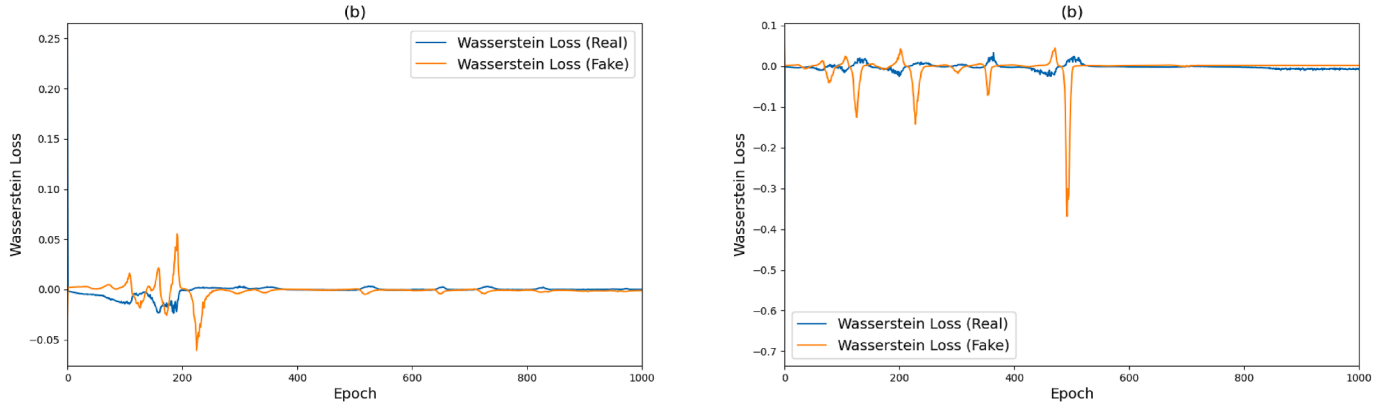

(a) S2 (b) S4

Fig. 26. Wasserstein loss plots for the sensor combinations.

terns in both real and synthetic data. The adversarial aspect of the AAE contributes to the robustness of the model by distinguishing between genuine and synthetic data during the training phase. This adversarial training helps enhance the quality of the fused features, ensuring that they retain valuable information while minimising noise and irrelevant details. The AAE is trained with both real and synthetic data, which facilitates the AAE in learning a comprehensive representation that is both informative and generalizable. Tests are conducted using only real data to evaluate how well the model captures real-world patterns.

Fig. 27 illustrates the WGAN-AAE's application to data across various combinations (utilising one, two, three, four, five, and six sensors) for both real and synthetic datasets.

Figs. 28 and 29 demonstrate the performance of WGAN-AAE on fused signals through three key loss plots for different combinations of sensors (one and six sensors):

- The sub-figure (a) shows the decreasing trend of the reconstruction loss, indicating the WGAN-AAE's ability to effectively compress original signals into a 300-point representation for the fused signals.
- The sub-figure (b) illustrates a diminishing generator loss, signifying the WGAN-AAE's proficiency in generating synthetic fused signals that closely align with the characteristics of the real fused signals.
- The sub-figure (c) depicts a decreasing discriminator loss, indicating the WGAN-AAE's success in generating fused signals that are challenging for the discriminator to differentiate from real fused signals.

5.3. Classification results

The effect of sensor placement and orientation on classification performance was evaluated using a series of classification tasks for pressure, flow rate, leakage size, and leakage location. Through repeated training and testing, classifiers were developed for different flow and leakage characteristics across multiple datasets. The purposes of this section are to present the results of the classification accuracies and to examine the influence of sensor configuration on performance. A total of 63 unique sensor configurations were created by combining all possible combinations of the six sensors deployed on the testbed. Each classification task involved the evaluation of all 63 configurations for a single label (pressure, flow rate, leakage size, or location). Using the same approach, multiple parameters were considered simultaneously in the multi-label classification task. In total, this resulted in $4 \times 63 + 63 = 315$ classification scenarios, accounting for four single-label and one multi-label classification problems. As mentioned before, the paper uses 70 % of the data for training and 30 % held out for testing, with 10-fold cross-validation applied during model evaluation.

5.3.1. Flow rate classification

This section discusses optimal sensor configurations and numbers, along with an evaluation of flow rate classifiers' effectiveness. Table 7 presents the top ten sensor configurations for binary flow-rate classification, listing the sensors used, training accuracy (± std), and test metrics (accuracy and F1 [13]). Configurations are ranked from 1 to 10, with the top-performing layout (1,2,3,4,6) achieving 91.04 % ± 0.90 % test accuracy with F1 = 90.32 % ± 1.06 %. Across the top ten configurations, accuracy ranges from 88.85 % to 91.04 %, with F1 score closely tracking (≈ 88.30 %-90.32 %), indicating balanced precision-recall trade-offs under mild class imbalance. As demonstrated in the table, S2 consistently appears across all ten ranks, underscoring the notable efficacy of S2 in the flow rate classification. The recurrent presence of S2 in the top-ranking configurations suggests its substantial impact on achieving high classification performance. S2 contributes significantly to the accuracy and stability of flow rate classification models, positioning it as an essential part of their success across various sensor combinations.

Table 8 illustrates the sensor combinations within the top 30 ranks, highlighting that configurations involving three and four sensors emerge as particularly effective for achieving optimal results. According to the data presented, these combinations are highly significant in delivering high-ranking outcomes for the study. Based on this insight, three or four sensors are highly effective in maximizing flow rate classification, as evidenced by their prevalence in the top-performing configurations. Additionally, the table reveals that configurations with only one sensor and those incorporating six sensors have the lowest ranks. This observation leads to the conclusion that relying on a single sensor may not capture all informative data, and the use of six sensors might introduce correlations that impact the classification outcomes negatively.

5.3.2. Pressure classification

This section presents an evaluation of the effectiveness of pressure classifiers and discusses the optimal selection of the number of sensors and sensor configurations for pressure classification. Table 9 encapsulates the outcomes of a pressure classification study, highlighting the top ten ranking results and their corresponding variations in performance trends. The configurations are assessed based on the sensors employed, training accuracy with standard deviation, and testing accuracy and F1 with standard deviation. Rankings range from 1 to 10, with the top-performing configuration listed first. The best layout $(1, 2, 3, 4, 5)$ achieved a test accuracy of 98.69 % ± 0.93 % and an F1 score of 98.64 % ± 1.02 %.The lowest accuracy achieved was 78 %. These results highlight a broad range of classification accuracy, emphasizing the importance of specific sensor configurations for optimal performance. As demonstrated in the table, S2 consistently appears across all ten ranks,

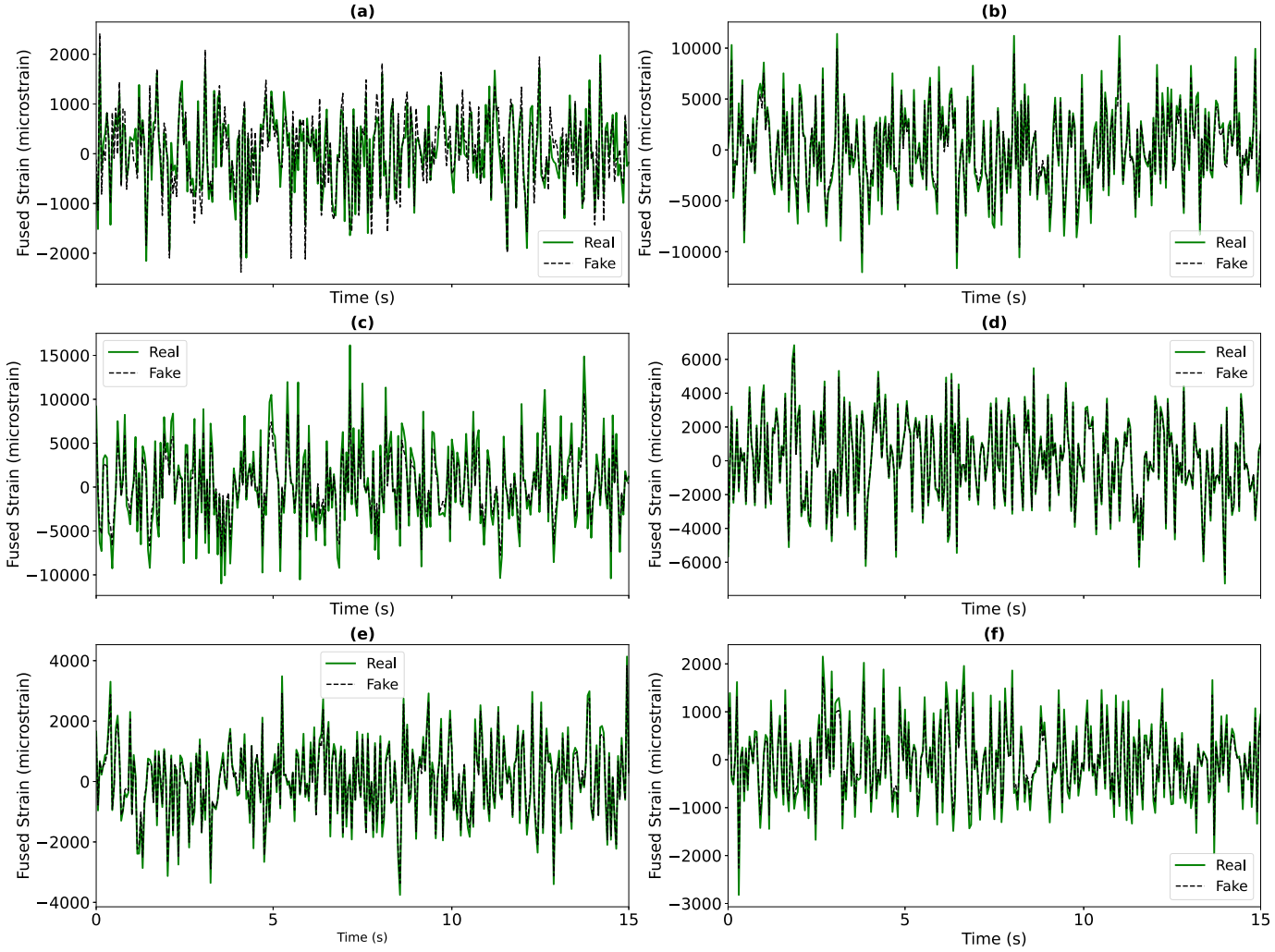

Fig. 27. Signal Fusion with the WGAN-AAE approach: Condensing datasets from various sensor configurations to 300 informative points. (a) One sensor: 15,000 to 300 points, (b) Two sensors: 30,000 to 300 points, (c) Three sensors: 45,000 to 300 points, (d) Four sensors: 60,000 to 300 points, (e) Five sensors: 75,000 to 300 points, (f) Six sensors: 90,000 to 300 informative fused data points.

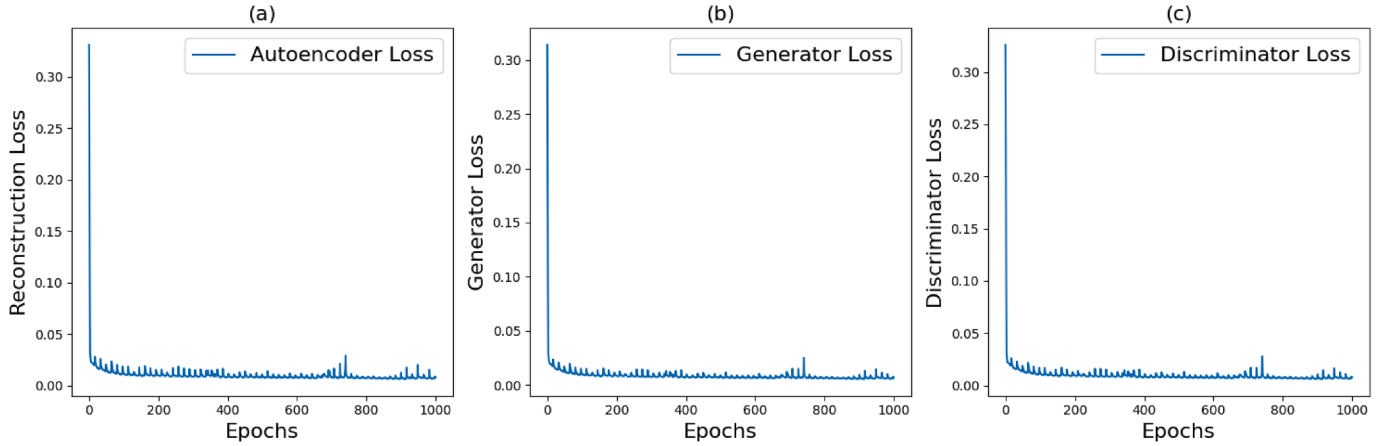

Fig. 28. WGAN-AAE's efficacy in compressing and generating fused signals was revealed in decreasing (a) Reconstruction, (b) Generator, and (c) Discriminator losses for one sensor.

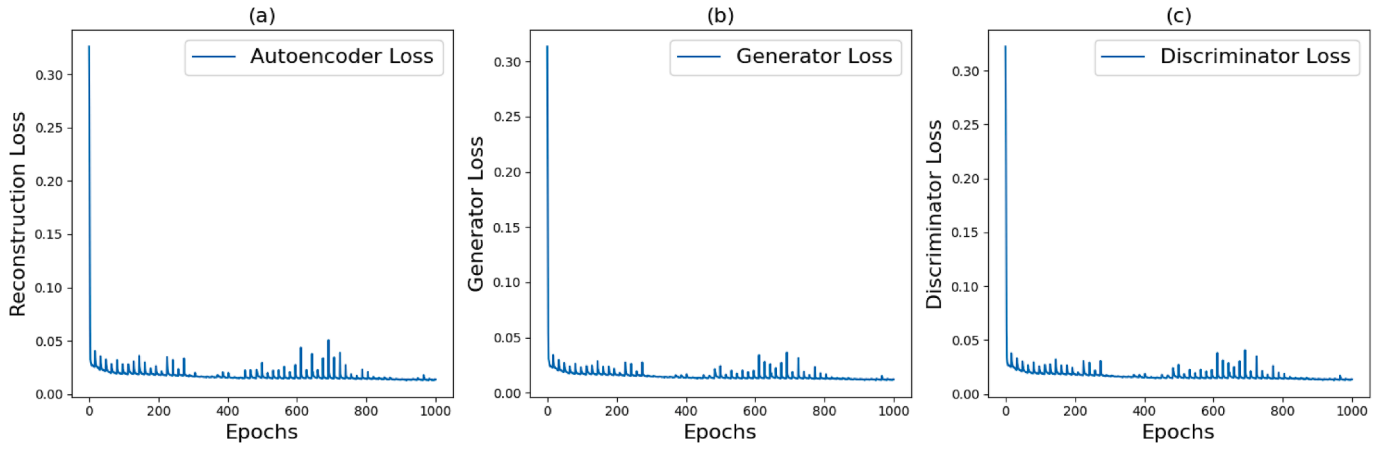

Fig. 29. WGNA-AAE's efficacy in compressing and generating fused signals was revealed in decreasing (a) Reconstruction, (b) Generator, and (c) Discriminator losses for six sensors.

Table 7
Top ten sensor configurations for flow-rate classification (with Test Acc and F1).

Rank	Used sensors	Train Acc ± std (%)	Test Acc ± std (%)	Test F1 ± std (%)
1	1, 2, 3, 4, 6	98.11±1.01	91.04±0.90	90.32±1.06
2	2, 3, 4, 6	98.22±1.21	90.94±0.97	90.18±1.08
3	2, 3, 6	98.12±1.14	90.65±0.95	90.04±1.10
4	2, 3, 4	97.42±1.14	90.55±0.99	89.99±1.12
5	3, 4, 6	97.31±1.19	90.55±0.98	89.95±1.11
6	1, 2, 4	98.18±1.25	90.05±1.21	89.34±1.15
7	2, 6	97.92±1.34	89.72±1.19	89.35±1.16
8	1, 2, 6	97.13±1.21	89.35±1.20	88.85±1.18
9	4, 6	97.13±1.31	88.85±1.27	88.40±1.20
10	1, 2, 3, 4	97.00±1.07	88.85±1.39	88.30±1.22

Table 8
Number of appearances of instances with different numbers of sensors in the 30 top-ranking flow rate classifiers.

Number of Sensors	One sensor	Two sensors	Three sensors	Four sensors	Five sensors	Six sensors
Number of Appearances	1	4	8	11	5	1

Table 9
Top ten configurations for binary pressure classification.

Rank	Used sensors	Training accuracy ± std (%)	Testing accuracy ± std (%)	Testing F1 ± std (%)
1	1, 2, 3, 4, 5	99.10±0.91	98.69±0.93	98.64±1.02
2	1, 2, 3, 5, 6	98.99±0.90	98.27±0.93	98.22±1.03
3	2, 3, 6	98.92±0.95	98.23±0.91	98.18±1.02
4	1, 2, 5	98.56±0.81	97.98±0.91	97.93±1.03
5	1, 2, 3, 6	97.99±1.03	97.89±0.92	97.84±1.02
6	4, 5, 6	98.53±1.00	97.89±0.93	97.84±1.02
7	1, 2, 5, 6	98.75±0.93	97.77±1.01	97.72±1.03
8	1, 2, 3	98.79±0.93	97.76±0.90	97.71±1.02
9	1, 2, 4	98.90±1.02	97.76±1.05	97.71±1.03
10	2, 6	98.80±0.97	97.75±0.90	97.70±1.02

underscoring the notable efficacy of S2 in the pressure classification. The recurrent presence of S2 in the top-ranking configurations suggests its substantial impact on achieving high classification performance. This observation underscores the significance of S2 in contributing to the accuracy and stability of the pressure classification models, positioning it as a crucial component in the success of these classifiers across various sensor combinations.

Table 10 illustrates the sensor combinations within the top 30 ranks, highlighting that configurations involving three and four sensors emerge as particularly effective for achieving optimal results. The data presented underscores the significance of these specific combinations, indicating their prominence in delivering high-ranking outcomes within the context of the study. This insight emphasizes the importance of carefully selecting and incorporating three or four sensors to maximize the effectiveness of the pressure classification, as evidenced by their prevalence in the top-performing configurations. Additionally, the table reveals that configurations with only one sensor and those incorporating six sensors have the lowest ranks. This observation leads to the conclusion that relying on a single sensor may not capture all informative data, and using six sensors may introduce correlations that negatively impact classification outcomes.

5.3.3. Leakage size and location classification

This section evaluates the performance of classifiers developed for detecting leakage size and explores the optimal number and configuration of sensors required for accurate classification. Across all configura-

Table 10
Number of appearances of instances with different numbers of sensors in the 30 top-ranking pressure classifiers.

Number of Sensors	One sensor	Two sensors	Three sensors	Four sensors	Five sensors	Six sensors
Number of Appearances	1	2	10	9	7	1

Table 11
Top ten configurations for leakage-location classification.

Rank	Used sensors	Training accuracy ± std (%)	Testing accuracy ± std (%)	Testing F1 ± std (%)
1	1, 2, 3, 4, 6	98.47±1.01	91.22±0.98	90.60±1.05
2	1, 2, 6	98.33±1.23	90.40±1.02	89.85±1.08
3	1, 2, 4, 6	98.29±1.11	90.40±1.11	89.80±1.16
4	1, 2, 3, 4, 6	98.13±1.34	90.40±1.15	89.78±1.20
5	2, 3, 4, 5	98.19±1.00	89.43±1.00	88.70±1.05
6	2, 5, 6	98.19±1.10	89.57±1.00	88.85±1.05
7	1, 2, 3	97.11±1.09	89.00±0.98	88.30±1.03
8	2, 4, 5, 6	98.01±1.07	88.99±0.90	88.20±0.98
9	1, 3, 5	98.01±1.05	88.90±1.04	88.10±1.10
10	1, 5, 4	97.98±1.21	88.89±1.04	88.05±1.10

tions, testing accuracy ranged from 93 % to 100 %, and several compact layouts achieved perfect (100 %) accuracy with zero variance. In particular, the following used sensor sets reached 100 %: 1,2,4,5; 1,3,5; 2,5; 1,5; 3,5; 4,5; 5,6; 4,5,6; 1,4,5; and 1,2,5. These findings show that leakage size leaves a strong, distinguishable imprint on the strain response, enabling reliable magnitude discrimination even with minimal sensor counts, provided placements capture the dominant strain effects.

Another purpose of this section is to provide an assessment of the effectiveness of leakage location classifiers and to discuss the optimal selection of the number of sensors and sensor configurations for leakage location classification. Table 11 presents the outcomes of a leakage location classification study, highlighting the top ten ranking results and their corresponding variations in performance trends. The configurations are assessed based on the sensors employed, training accuracy with standard deviation, and testing accuracy with standard deviation. Rankings range from 1 to 10, with the top-performing configuration listed first. The best layout, $(1, 2, 3, 4, 6)$, attains Acc = $91.22\,\% \pm 0.98\,\%$ with F1 = $90.45\,\% \pm 1.04\,\%$ and a training accuracy of $98.47\,\% \pm 1.01\,\%$. The lowest accuracy achieved was 72 %. These results highlight a broad range of classification accuracy, emphasizing the importance of specific sensor configurations for optimal performance. As demonstrated in the table, S2 consistently appears across all ten ranks, underscoring the notable efficacy of S2 in the leakage location classification. The recurrent presence of S2 in the top-ranking configurations suggests its substantial impact on achieving high classification performance. This observation underscores the significance of S2 in contributing to the accuracy and stability of the leakage location classification models, positioning it as a crucial component in the success of these classifiers across various sensor combinations.

Table 12 illustrates the sensor combinations within the top 30 ranks, highlighting that configurations involving three and four sensors emerge as particularly effective for achieving optimal results. The data presented underscores the significance of these specific combinations, indicating their prominence in delivering high-ranking outcomes within the context of the study. This insight emphasizes the importance of carefully selecting and incorporating three, four, and five sensors to maximize the effectiveness of the leak location classification, as evidenced by their prevalence in the top-performing configurations. Additionally, the table reveals that configurations with only one sensor and those incorporating six sensors have the lowest ranks. Based on this observation, we conclude that relying on a single sensor may not capture all informative data, and the use of six sensors may introduce correlations that influence classification outcomes negatively.

5.3.4. Multi-label classification

Multi-label classification allows each instance to belong to multiple classes simultaneously, better reflecting real-world complexity than single-label schemes. This flexibility makes it effective for extracting meaningful insights from heterogeneous datasets. In our context, a single sample may be assigned labels for pressure, flow rate, leakage size, and leakage location at once. By modelling the probability of membership across multiple labels, the approach captures interdependent attributes and provides a comprehensive, realistic representation of the underlying relationships.

Table 13 lists the outcomes of the multi-label classification study, highlighting the top twenty ranking results and their corresponding variations in performance trends. The configurations are assessed based on the sensors employed, training accuracy with standard deviation, and testing accuracy with standard deviation. Rankings range from 1 to 20, with the top-performing configuration listed first. The best layout, $(2, 3, 4, 5, 6)$, attains (Acc = $94.89\,\% \pm 1.13\,\%$, F1 = $94.20\,\% \pm 1.18\,\%$). The lowest accuracy achieved was 70 %. These results highlight a broad range of classification accuracy, emphasizing the importance of specific sensor configurations for optimal performance. The table illustrates the consistency of S2 and S3 across all ten rankings, illustrating their significant efficacy in determining leakage locations. It appears that S2 and S3 have a substantial impact on achieving high classification performance, given their regular presence in the top-ranking configurations. A critical component of the success of these classifiers across different sensor combinations is S2 and S3 contributing to the accuracy and stability of the leakage location classification models.

Table 14 illustrates the sensor combinations within the top 40 ranks, highlighting that configurations involving two and three sensors emerge as particularly effective for achieving optimal results. The data presented underscores the significance of these specific combinations, indicating their prominence in delivering high-ranking outcomes within the context of the study. This insight emphasizes the importance of carefully selecting and incorporating three and four sensors to maximise the effectiveness of the multi-label classification, as evidenced by their prevalence in the top-performing configurations. Moreover, the table indicates that configurations with only one sensor and those incorporating six sensors have the lowest rankings. Based on this observation, it can be concluded that relying on a single sensor may not capture all informative data, while using six sensors may introduce correlations that negatively impact classification results.

Table 12
Number of appearances of instances with different numbers of sensors in the 30 top-ranking leak location classifiers.

Number of Sensors	One sensor	Two sensors	Three sensors	Four sensors	Five sensors	Six sensors
Number of Appearances	1	4	7	10	7	1

Table 13
Top twenty configurations for multi-label classification.

Rank	Used sensors	Training accuracy ± std (%)	Testing accuracy ± std (%)	Testing F1 (micro) ± std (%)
1	2, 3, 4, 5, 6	98.76±1.15	94.89±1.13	94.20±1.18
2	1, 2, 3, 6	98.64±1.43	94.88±1.40	94.18±1.45
3	2, 3, 6	98.51±1.00	94.88±1.33	94.16±1.36
4	2, 3, 4, 6	98.50±1.17	94.48±1.19	93.80±1.23
5	1, 2, 3, 6	97.84±1.23	94.00±1.10	93.35±1.15
6	1, 2, 4, 5	97.80±1.39	93.89±1.11	93.25±1.16
7	2, 6	97.87±1.00	93.19±1.00	92.55±1.05
8	3, 4, 6	97.80±1.01	93.18±1.00	92.55±1.05
9	2, 3	97.80±0.98	93.00±0.99	92.35±1.04
10	1, 2, 4	97.80±1.00	93.00±1.00	92.34±1.05
11	1, 2, 5, 6	98.23±1.10	91.85±1.20	91.20±1.25
12	3, 6	98.15±1.21	91.82±1.11	91.15±1.16
13	2, 4, 6	97.00±1.00	91.70±1.14	91.00±1.19
14	1, 3, 4	97.20±1.30	91.63±1.09	90.95±1.14
15	3, 4	97.00±1.07	91.46±1.14	90.80±1.19
16	5, 6	97.00±1.20	91.46±1.24	90.78±1.29
17	1, 2, 3, 4, 5, 6	97.20±1.00	91.43±1.38	90.75±1.43
18	1, 6	97.86±1.35	91.00±1.29	90.30±1.34
19	4, 6	97.89±1.05	90.99±1.43	90.28±1.48
20	1, 2, 3, 4	97.32±1.00	90.64±1.59	89.95±1.64

Table 14
Number of appearances of instances with different numbers of sensors in the 40 top-ranking multi-label classifiers.

Number of Sensors	One sensor	Two sensors	Three sensors	Four sensors	Five sensors	Six sensors
Number of Appearances	1	10	15	8	5	1

6. Comparative analysis

This Section presents the benchmarking of the leakage-location task, reporting test accuracy for three variants shown in Table 15: WGAN + AAE, GAN + AAE, and WGAN + Concatenation. This design isolates the contribution of (i) the Wasserstein critic (by comparing WGAN + AAE to GAN + AAE) and (ii) learned feature-level fusion and latent regularisation (by comparing WGAN + AAE to WGAN + Concatenation).

The rationale for each component is as follows. The WGAN critic optimises the Wasserstein distance and, with standard Lipschitz controls, provides smooth, informative gradients that mitigate mode collapse (a common phenomenon in GANs training) and improve training stability in small, noisy 1D FBG regimes [34,56]. The AAE applies domain-aware latent regularisation to match an explicit prior, shaping the latent space so that subtle operational regimes and anomalies become more separable; prior studies on AAE-based anomaly detection support the view that adversarial latent regularisation can enhance generalisation for such tasks [57,58]. By contrast, a standard VAE typically assumes an (isotropic) Gaussian prior and a Gaussian approximate posterior; when the underlying structure is multimodal, heavy-tailed, or otherwise non-Gaussian, especially in rare or noisy regimes, this misspecification can reduce anomaly-detection performance [58]. Finally, learned feature-level fusion (as used in WGAN + AAE) integrates synthetic and real signals within a shared representation, which is more effective than naïve concatenation (the WGAN + Concatenation baseline) for capturing operational variability and noise structure.

Across the sensor configurations (Table 15), WGAN + AAE consistently delivers the highest testing accuracy, establishing a clear baseline for subsequent analyses. For the strongest layout (1,2,3,4,6), WGAN + AAE reaches 91.22 % ± 0.98 %, compared with 89.38 % ± 1.06 % for GAN + AAE and 88.86 % ± 1.12 % for WGAN + Concatenation. The advantage persists across compact arrangements; for example, on (1,2,6) the results are 90.40 % ± 1.02 % (WGAN + AAE), 88.62 % ± 1.09 % (GAN + AAE), and 88.08 % ± 1.15 % (WGAN + Concatenation). Even in the smallest observed margin (2,5,6), WGAN + AAE still leads by 0.78 percentage points. Averaged over all ten configurations, WGAN + AAE outperforms GAN + AAE by approximately 1.7 percentage points and WGAN + Concatenation by approximately 2.3 percentage points, supporting the claim that Lipschitz-constrained adversarial synthesis, domain-aware latent regularisation, and learned feature-level fusion yield superior leakage-location accuracy compared with either replacing WGAN with a standard GAN or forgoing learned fusion.

7. Discussions

The strain signals recorded by the sensors display distinct and consistent patterns that can be analyzed to infer characteristics related to pipe flow and leakage. These patterns remain stable even when individual parameters are varied, regardless of other flow or leakage conditions. Among the examined factors, the maximum strain drop emerged as the most informative indicator. Three out of the four evaluated parameters-flow rate, pressure, and leakage size-showed a direct influence on the magnitude of this drop. An increase of 5 GPM in flow rate corresponded to an approximate 6 % reduction in the maximum strain drop. In contrast, pressure demonstrated an inverse relationship, where each 0.2 bar increase resulted in roughly a 20 % increase in the strain drop. Leakage size had the most significant impact, with a large leakage producing

Table 15
Testing accuracy of WGAN + AAE, GAN + AAE, and WGAN + Concatenation across different sensor combinations (leakage location classification).

Used sensors	WGAN + AAE	GAN + AAE	WGAN + Concat.
1, 2, 3, 4, 6	**91.22 ± 0.98**	89.38 ± 1.06	88.86 ± 1.12
1, 2, 6	**90.40 ± 1.02**	88.62 ± 1.09	88.08 ± 1.15
1, 2, 4, 6	**90.40 ± 1.10**	88.58 ± 1.18	88.04 ± 1.24
1, 2, 3, 4, 6	**90.40 ± 1.15**	88.55 ± 1.22	87.99 ± 1.28
2, 3, 4, 5	**89.43 ± 1.00**	87.70 ± 1.09	87.18 ± 1.14
2, 5, 6	**89.57 ± 1.01**	88.79 ± 1.07	87.27 ± 1.13
1, 2, 3	**89.00 ± 0.98**	87.26 ± 1.05	86.73 ± 1.11
2, 4, 5, 6	**88.99 ± 0.90**	87.21 ± 0.97	86.69 ± 1.03
1, 3, 5	**88.90 ± 1.04**	87.11 ± 1.11	86.60 ± 1.15
1, 5, 4	**88.89 ± 1.04**	87.10 ± 1.17	86.58 ± 1.17

about 55 % more strain drop than a small one. While leakage location did not directly alter the maximum strain drop, it affected the time required for the strain signal to stabilize, depending on the sensor's proximity to the leak. Certain properties were found to be interrelated-for instance, greater distances between the leakage point and sensors reduced the influence of flow rate changes. These quantified effects are specific to the tested pipeline. Both longitudinal and circumferential sensors displayed consistent responses to variations in flow parameters. However, circumferential sensors exhibited greater gain, enhancing sensitivity and reducing the relative impact of noise, thus improving the overall reliability of the measurements.

Leakage size classification proved to be readily attainable, achieving results with up to 100 % ±0.00 % accuracy for most sensor configurations. Pressure classification followed suit with commendable outcomes, reaching a testing accuracy of 98.69 % ± 0.93 % and maintaining high accuracy across a diverse range of sensor configurations. Flow rate classification also yielded favorable results, attaining an accuracy of 91.04 % ± 0.90 % with appropriate settings. Leakage location classification was accomplished with good results, reaching an accuracy of 91.22 % ± 0.98 % with the use of an ample number of sensors to achieve these outcomes. Also, we explore the application of multi-label classification to comprehensively consider the probabilities associated with various aspects of pipelines in the real world. The multi-label class classification was accomplished with good results, reaching an accuracy of 94.89 % ± 1.13 %.

In the case of leakage location classification, a significant gap was observed between training and testing accuracies, indicating potential overfitting of the classifier. Despite efforts to mitigate this-such as training with a reduced dataset comprising 70 % of the real and synthetic data-the issue persisted. A likely explanation is that the signal variations caused by changes in leakage location were too subtle and lacked consistency, making it difficult for the classifier to generalize effectively. The limitations of the testbed may have contributed to this challenge. Expanding the experimental setup could improve classification performance by amplifying and standardizing the signal differences associated with leakage at various positions. Moreover, the distinguishing features related to leakage location were inherently time-dependent. As a result, these features may have been diminished during the denoising process, particularly by the application of the moving average filter, which was necessary to suppress noise in the recorded signals.

The classification results for pressure and flow rate revealed that high accuracy could be achieved using a relatively small number of sensors. Although some studies suggest that increasing the number of sensors generally improves performance, our findings indicate that a reduced sensor set can still provide accurate, reliable and cost-effective damage detection [59]. In this study, a minimal sensor configuration was sufficient to yield consistent and accurate outcomes, which aligns with observations in related works [60]. This effectiveness may be attributed to the relatively straightforward and distinguishable patterns associated with pressure and flow rate variations, making them easier to classify without the need for extensive sensor coverage. In contrast, incorporating additional sensors may introduce unnecessary complexity. However, when scaling the monitoring system to cover larger pipeline networks, more sensors would naturally be required-potentially increasing the likelihood of sensor faults. To maintain system reliability in such cases, sensor fault diagnosis techniques, such as the Bayesian approach proposed by Huang et al. [61], could be integrated to preserve the integrity of the sensor network.

Table 16
Number of appearances of each sensor in the 50 top-ranking classifiers.

Classification type	S1	S2	S3	S4	S5	S6
Flow rate classifiers	20	35	17	33	15	24
Pressure classifiers	23	30	29	18	24	21
Leakage location classifiers	20	25	20	38	17	20
Leakage size classifiers	19	34	29	20	16	21
Multi-label classifiers	20	37	24	20	14	28

Analyzing the temperature-compensated FBG strain data enables the differentiation between signal changes resulting from actual leak events and those influenced by environmental factors or boundary conditions. This distinction was also explored in the study by Chen et al. [62], where SVM classifiers were developed to differentiate pressure drops caused by NPWs from those caused by external disturbances. Regarding sensor performance, the experimental findings highlighted the enhanced effectiveness of circumferentially mounted sensors across all classification tasks. Their improved sensitivity is primarily attributed to higher signal gain, which helps preserve critical information during the noise reduction process and amplifies signal variations under varying flow and leakage conditions. For leakage location classification, sensor placement played a pivotal role; sensors installed near the center of the pipe yielded higher accuracy, likely due to their balanced exposure to leakage signals from different positions along the pipeline. The applicability of this monitoring technique to real-world pipeline systems is supported by the use of FBG sensors, which offer advantages such as multiplexing capabilities-allowing multiple sensors to be linked along a single optical fiber. Additionally, FBG systems support long-range monitoring (up to 250 km) due to low signal attenuation in optical fibers [63]. Temperature-compensated FBG sensors further enhance reliability by mitigating strain changes caused by thermal effects, enabling consistent monitoring under varying environmental conditions.

Additionally, it is noteworthy that achieving high-accuracy results in comparison with previous studies [6] is inherent in the approach, which involves leveraging WGAN for training and incorporates a novel fusion of real and synthetic data. By utilizing WGAN, our objective is to enhance the diversity and realism of the dataset, thereby improving the model's ability to discern intricate patterns in the data. The fusion of real and synthetic data contributes to a more robust understanding of the complexities within the pipeline domain. Furthermore, the paper emphasizes the identification and incorporation of the most informative features, optimizing the model's ability to accurately predict both simple and multi-label classifications. Through these strategies, our aim is to attain heightened accuracy in capturing the nuanced relationships within real-world pipeline scenarios.

Table 16 provides a comprehensive overview of the frequency of each sensor's appearance (S1 to S6) within the top 50 classifiers across distinct classification types. The numerical entries in the table denote the count of instances where a particular sensor is utilized among the top 50 classifiers for a given classification type. For instance, in the flow rate classifiers, pressure classifiers, leakage location classifiers, leakage size classifiers, and multi-label classifiers, the maximum appearances of each sensor are as follows: S2 with 35 times, S2 with 30 times, S4 with 38 times, S2 with 34 times, and S2 with 37 times.

8. Conclusions

This study quantified the effect of pipeline leaks on FBG strain responses and introduced a new data-fusion methodology to detect and localise leaks under limited, noisy, and variable operating conditions. Controlled experiments on a 6 m long steel pipeline showed that leak-induced strain drops increased with pressure, decreased with higher flow, and grew with leak size, while leak location primarily affected temporal dynamics (stabilisation time) rather than the drop magnitude itself. Because these effects can be subtle and interdependent, simple visual inspection is insufficient for reliable assessment. To address this, we proposed a hybrid WGAN-AAE fusion framework that (i) synthesises signals via a Wasserstein GAN, (ii) performs domain-aware latent regularisation and learns feature-level fusion with an adversarial autoencoder, and (iii) uses a 2D-CNN for classification (binary and multi-label settings based on BR). Trained on 70 % real data augmented with WGAN samples and evaluated on the held-out 30 %, the framework achieved 94.89 % ± 1.13 % multi-label accuracy. Single-label results were 100 % ± 0.00 % (leak size), 98.69 % ± 0.93 % (pressure), 91.04 % ± 0.90 % (flow), and 91.22 % ± 0.98 % (leak location). Comparative evaluation across the ten best sensor layouts, WGAN + AAE consistently outperformed GAN + AAE and a WGAN-concatenation baseline, underscoring the benefits of Wasserstein synthesis, latent regularisation, and learned fusion. The results indicated that accurate and robust sensor-based monitoring for leak detection and localisation is feasible in pipeline systems with limited datasets as well as noisy and variable operation conditions. Future work is planned to test the pre-trained model on different pipeline systems, extend validation to longer assets and real field conditions, and evaluate performance on unseen domains via transfer learning with targeted fine-tuning. While the current model was optimised for FBG strain sensors for markedly different sensors or lower data quality, future work will apply modest domain-specific fine-tuning and rigorous quality control (QC), including denoising, dropout handling, calibration checks, sensor bonding/installation verification, and drift monitoring prior to evaluation. In particular, the model trained on the real dataset will be fine-tuned on entirely unseen datasets to adapt the representations and decision layers to new domains with minimal additional data.

CRediT authorship contribution statement

Sahar Hassani: Writing – review & editing, Writing – original draft, Visualization, Validation, Software, Resources, Methodology, Investigation, Formal analysis, Data curation, Conceptualization; **Samir Mustapha:** Writing – review & editing, Data curation, Conceptualization, Visualization; **Mohsen Mousavi:** Writing – review & editing, Visualization, Software, Conceptualization; **Jianchun Li:** Writing – review & editing, Supervision, Project administration, Conceptualization; **Chongmin Song:** Writing – review & editing, Supervision, Project administration, Conceptualization; **Ulrike Dackermann:** Writing – review & editing, Visualization, Supervision, Project administration, Resources, Funding acquisition, Conceptualization.

Data availability

The data that has been used is confidential.

Declaration of competing interest

The authors declare that they have no known competing financial interests or personal relationships that could have appeared to influence the work reported in this paper.

Acknowledgement

Dr Samir Mustapha would like to acknowledge the financial support of the University Research Board at the American University of Beirut (Award#103604)

References

[1] G.A. Papadakis, Assessment of requirements on safety management systems in EU regulations for the control of major hazard pipelines, J. Hazard. Mater. 78 (1–3) (2000) 63–89.
[2] D. Lyons, Western European Cross-Country Oil Pipelines 30-year Performance Statistics, Concawe Brussels, Belgium, 2002.
[3] J.L. Kennedy, Oil and gas pipeline fundamentals, International Journal of Pressure Vessels and Piping, 87 (7) (2010) 373–380. https://doi.org/10.1016/j.ijpvp.2010.04.003
[4] H.A. Kishawy, H.A. Gabbar, Review of pipeline integrity management practices, Int. J. Press. Vessels Pip. 87 (7) (2010) 373–380 https://doi.org/10.1016/j.ijpvp.2010.04.003 https://www.sciencedirect.com/science/article/pii/S0308016110000827.
[5] A. Lubben, The Keystone oil spill no one's talking about will be nearly impossible to clean up, 2019.
[6] M. Saade, S. Mustapha, Assessment of the structural conditions in steel pipeline under various operational conditions–a machine learning approach, Measurement 166 (2020) 108262.
[7] J.P. Lynch, C.R. Farrar, J.E. Michaels, Structural health monitoring: technological advances to practical implementations [scanning the issue], Proc. IEEE 104 (8) (2016) 1508–1512.
[8] H. Jin, L. Zhang, W. Liang, Q. Ding, Integrated leakage detection and localization model for gas pipelines based on the acoustic wave method, J. Loss Prev. Process Ind. 27 (2014) 74–88.
[9] M.V. Casillas Ponce, L.E. Garza Castanon, V.P. Cayuela, Model-based leak detection and location in water distribution networks considering an extended-horizon analysis of pressure sensitivities, J. Hydroinf. 16 (3) (2014) 649–670.
[10] V.V. Spirin, M.G. Shlyagin, S.V. Miridonov, F.J.M. Jimenez, R.M.L. Gutierrez, Fiber bragg grating sensor for petroleum hydrocarbon leak detection, Opt. Lasers Eng. 32 (5) (1999) 497–503.
[11] J.-R. Lee, H. Tsuda, Fiber optic liquid leak detection technique with an ultrasonic actuator and a fiber bragg grating, Opt Lett 30 (24) (2005) 3293–3295.
[12] S. Mustapha, A. Braytee, L. Ye, Multisource data fusion for classification of surface cracks in steel pipes, J. Nondestruct. Eval. Diagnos. Prognos. Eng. Syst. 1 (2) (2018) 021007–021007.
[13] S. Hassani, S. Mustapha, J. Li, M. Mousavi, U. Dackermann, Next-generation coupled structure-human sensing technology: enhanced pedestrian-bridge interaction analysis using data fusion and machine learning, Inf. Fus. 118 (2025) 102983.
[14] S. Hassani, U. Dackermann, M. Mousavi, S. Mustapha, J. Li, AAE-CycleWGAN fusion framework for generating fused strain data from sparse to dense domains in bridge monitoring systems, Inf. Fus. (2025) 103736.
[15] T. Mahmood, J. Li, Y. Pei, F. Akhtar, A. Imran, K.U. Rehman, A brief survey on breast cancer diagnostic with deep learning schemes using multi-image modalities, IEEE Access 8 (2020) 165779–165809.
[16] A. Rehman, T. Mahmood, T. Saba, Robust kidney carcinoma prognosis and characterization using Swin-ViT and deeplabV3 + with multi-model transfer learning, Appl. Soft Comput. 170 (2025) 112518.
[17] A.M. Ali, B. Benjdira, A. Koubaa, W. Boulila, W. El-Shafai, TESR: two-stage approach for enhancement and super-resolution of remote sensing images, Remote Sens. 15 (9) (2023) 2346.
[18] T. Mahmood, T. Saba, A. Rehman, F.S. Alamri, Harnessing the power of radiomics and deep learning for improved breast cancer diagnosis with multiparametric breast mammography, Expert Syst. Appl. 249 (2024) 123747.
[19] T. Mahmood, A. Rehman, T. Saba, Y. Wang, F.S. Alamri, Alzheimer's disease unveiled: cutting-edge multi-modal neuroimaging and computational methods for enhanced diagnosis, Biomed. Signal Process. Contr. 97 (2024) 106721.
[20] T. Mahmood, T. Saba, A. Rehman, Breast cancer diagnosis with MFF-Histonet: a multi-modal feature fusion network integrating CNNs and quantum tensor networks, J. Big Data 12 (1) (2025) 60.
[21] T. Mahmood, T. Saba, S. Al-Otaibi, N. Ayesha, A.S. Almasoud, AI-driven microscopy: cutting-edge approach for breast tissue prognosis using microscopic images, Microsc. Res. Tech. 88 (5) (2025) 1335–1359.
[22] U. Rajasekaran, M. Kothandaraman, A novel custom one-dimensional time-series densenet for water pipeline leak detection and localization using acousto-optic sensor, IEEE Access (2024).
[23] U. Rajasekaran, M. Kothandaraman, Comparative analysis of machine learning and deep learning based water pipeline leak detection using EDFL sensor, J. Pipeline Syst. Eng. Pract. 14 (4) (2023) 04023026.
[24] A. Khodayari-Rostamabad, J.P. Reilly, N.K. Nikolova, J.R. Hare, S. Pasha, Machine learning techniques for the analysis of magnetic flux leakage images in pipeline inspection, IEEE Trans. Magn. 45 (8) (2009) 3073–3084.
[25] X. Zhuang, S. Zhou, The prediction of self-healing capacity of bacteria-based concrete using machine learning approaches, Comput. Mater. Contin. 59 (1) (2019) 57–77.
[26] M. Luo, K. Wang, Z. Cai, A. Liu, Y. Li, C.F. Cheang, Using imbalanced triangle synthetic data for machine learning anomaly detection, Comput. Mater. Continua 58 (1) (2019).

[27] B. Xu, L. Tong, T. Bi-wan, H. Xin-jing, A continuous leakage real-time localization method based on space phase image of elastic wave field with improved CNN, Measurement 224 (2024) 113894.
[28] C. Zhang, B.J. Alexander, M.L. Stephens, M.F. Lambert, J. Gong, A convolutional neural network for pipe crack and leak detection in smart water network, Struct. Health Monitor. 22 (1) (2023) 232–244.
[29] S. Hassani, U. Dackermann, A systematic review of advanced sensor technologies for non-destructive testing and structural health monitoring, Sensors 23 (4) (2023) 2204.
[30] F. Conti, F. Madeo, A. Boiano, M. Tarabini, Electrical and mechanical data fusion for hydraulic valve leakage diagnosis, Meas. Sci. Technol. 34 (4) (2023) 044011.
[31] W. Xie, Y. Liu, X. Wang, J. Wang, The pipeline leak detection algorithm based on DS evidence theory and signal fusion mechanism, Alexandr. Eng. J. 85 (2023) 218–235.
[32] Y. Wang, J. Guo, Q. Shi, T. Hu, A crack detection method for pipelines using wavelet-based decision-level data fusion, IEEE Trans. Instrum. Meas. 72 (2023) 1–21.
[33] W. Yan, W. Liu, Q. Zhang, H. Bi, C. Jiang, H. Liu, T. Wang, T. Dong, X. Ye, Multi-source multi-modal feature fusion for small leak detection in gas pipelines, IEEE Sens. J. (2023).
[34] M. Arjovsky, S. Chintala, L. Bottou, Wasserstein generative adversarial networks, in: International Conference on Machine Learning, PMLR, 2017, pp. 214–223.
[35] S.P. Kok, Y.I. Go, X. Wang, M.L.D. Wong, Advances in fiber bragg grating (FBG) sensing: a review of conventional and new approaches and novel sensing materials in harsh and emerging industrial sensing, IEEE Sens .J. 24 (19) (2024) 29485–29505.
[36] S. Sfarra, C. Ibarra-Castanedo, F. Lambiase, D. Paoletti, A. Di Ilio, X. Maldague, From the experimental simulation to integrated non-destructive analysis by means of optical and infrared techniques: results compared, Meas. Sci. Technol. 23 (11) (2012) 115601.
[37] J.K. Sahota, N. Gupta, D. Dhawan, Fiber bragg grating sensors for monitoring of physical parameters: a comprehensive review, Opt. Eng. 59 (6) (2020) 060901–060901.
[38] I. Goodfellow, J. Pouget-Abadie, M. Mirza, B. Xu, D. Warde-Farley, S. Ozair, A. Courville, Y. Bengio, Generative adversarial networks, Commun. ACM 63 (11) (2020) 139–144.
[39] F. Luleci, F.N. Catbas, O. Avci, A literature review: generative adversarial networks for civil structural health monitoring, Front. Built Environ. 8 (2022) 1027379.
[40] I.J. Goodfellow, J. Pouget-Abadie, M. Mirza, B. Xu, D. Warde-Farley, S. Ozair, A. Courville, Y. Bengio, Generative adversarial nets, Adv. Neural Inf. Process. Syst. 27 (2014).
[41] A. Makhzani, J. Shlens, N. Jaitly, I. Goodfellow, B. Frey, Adversarial autoencoders, arXiv preprint arXiv:1511.05644. (2015).
[42] K. Berahmand, F. Daneshfar, E.S. Salehi, Y. Li, Y. Xu, Autoencoders and their applications in machine learning: a survey, Artif. Intell. Rev. 57 (2) (2024) 28.
[43] D. Bhatt, C. Patel, H. Talsania, J. Patel, R. Vaghela, S. Pandya, K. Modi, H. Ghayvat, CNN variants for computer vision: history, architecture, application, challenges and future scope, Electronics 10 (20) (2021) 2470.
[44] X. Zhao, L. Wang, Y. Zhang, X. Han, M. Deveci, M. Parmar, A review of convolutional neural networks in computer vision, Artif. Intell. Rev. 57 (4) (2024) 99.
[45] Z. Li, F. Liu, W. Yang, S. Peng, J. Zhou, A survey of convolutional neural networks: analysis, applications, and prospects, IEEE Trans. Neural Netw. Learn. Syst. 33 (12) (2021) 6999–7019.
[46] G. Tsoumakas, I. Katakis, Multi-label classification: an overview, Int. J. Data Warehous. Min. 3 (3) (2007) 1–13.
[47] M.-L. Zhang, Y.-K. Li, X.-Y. Liu, X. Geng, Binary relevance for multi-label learning: an overview, Front. Comput. Sci. 12 (2) (2018) 191–202.
[48] D. Ganda, R. Buch, A survey on multi label classification, Recent Trends Programm. Lang. 5 (1) (2018) 19–23.
[49] O. Luaces, J. Díez, J. Barranquero, J.J. del Coz, A. Bahamonde, Binary relevance efficacy for multilabel classification, Progr. Artif. Intell. 1 (4) (2012) 303–313.
[50] J. Read, B. Pfahringer, G. Holmes, E. Frank, Classifier chains for multi-label classification, in: Joint European Conference on Machine Learning and Knowledge Discovery in Databases, Springer, 2009, pp. 254–269.
[51] W. Cheng, E. Hüllermeier, K.J. Dembczynski, Bayes optimal multilabel classification via probabilistic classifier chains, in: Proceedings of the 27th International Conference on Machine Learning (ICML-10), 2010, pp. 279–286.
[52] E. Montanes, R. Senge, J. Barranquero, J.R. Quevedo, J.J. del Coz, E. Hüllermeier, Dependent binary relevance models for multi-label classification, Pattern Recognit. 47 (3) (2014) 1494–1508.
[53] T. Jiang, L. Ren, Z. Jia, D. Li, H. Li, Application of FBG based sensor in pipeline safety monitoring, Appl. Sci. 7 (6) (2017) 540.
[54] Z. Jia, L. Ren, H. Li, W. Sun, Pipeline leak localization based on FBG hoop strain sensors combined with BP neural network, Appl. Sci. 8 (2) (2018) 146.
[55] Natural resources canad (2020).
[56] Y. Kossale, M. Airaj, A. Darouichi, Mode collapse in generative adversarial networks: an overview, in: 2022 8th International Conference on Optimization and Applications (ICOA), IEEE, 2022, pp. 1–6.
[57] M. Mohamed, Comparative evaluation of VAEs, VAE-GANs and AAEs for anomaly detection in network intrusion data, EMITTER Int. J. Eng. Technol. 11 (2) (2023) 160–173.
[58] T. Kang, B.-J. You, J. Park, Y. Lee, A real-time anomaly detection method for robots based on a flexible and sparse latent space, Eng. Appl. Artif. Intell. 158 (2025) 111310.
[59] S.-W. Lin, T.-H. Yi, H.-N. Li, L. Ren, Damage detection in the cable structures of a bridge using the virtual distortion method, J. Bridge Eng. 22 (8) (2017) 04017039.
[60] I. Ahmad, M. Hussain, A. Alghamdi, A. Alelaiwi, Enhancing SVM performance in intrusion detection using optimal feature subset selection based on genetic principal components, Neural Comput. Appl. 24 (2014) 1671–1682.
[61] H.-B. Huang, T.-H. Yi, H.-N. Li, Bayesian combination of weighted principal-component analysis for diagnosing sensor faults in structural monitoring systems, J. Eng. Mech. 143 (9) (2017) 04017088.
[62] H. Chen, H. Ye, L.V. Chen, H. Su, Application of support vector machine learning to leak detection and location in pipelines, in: Proceedings of the 21st IEEE Instrumentation and Measurement Technology Conference (IEEE Cat. no. 04ch37510), 3, IEEE, 2004, pp. 2273–2277.
[63] M. Fernandez-Vallejo, S. Rota-Rodrigo, M. Lopez-Amo, Remote (250 km) fiber bragg grating multiplexing system, Sensors 11 (9) (2011) 8711–8720.